Title

Maximizing microbial bioproduction from sustainable carbon sources using iterative systems engineering

Permalink

https://escholarship.org/uc/item/18v2q3zn

Journal

Cell Reports, 42(9)

ISSN

2639-1856

Authors

Eng, Thomas
Banerjee, Deepanwita
Menasalvas, Javier
et al.

Publication Date

2023-09-01

DOI

10.1016/j.celrep.2023.113087

Cell Reports

Maximizing microbial bioproduction from sustainable carbon sources using iterative systems engineering

Graphical abstract

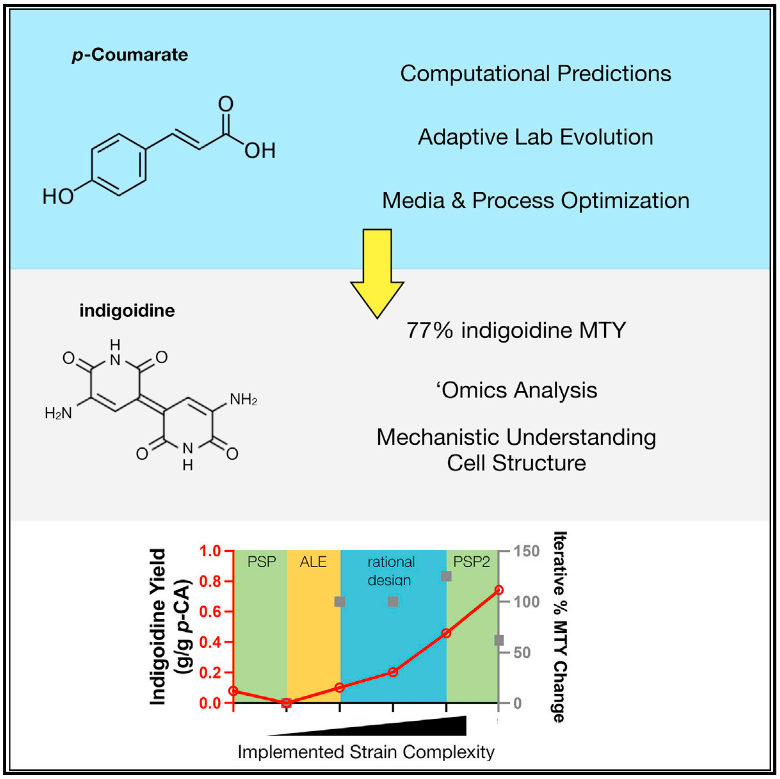

Highlights

- Bioconversion of 77% max theoretical yield of indigoidine from *para*-coumarate
- Rational engineering strategies are aided by computational modeling and proteomics data
- Adaptive lab evolution restores growth in initial computed strain design

Authors

Thomas Eng, Deepanwita Banerjee, Javier Menasalvas, ..., Jay D. Keasling, Christopher J. Petzold, Aindrila Mukhopadhyay

Correspondence

amukhopadhyay@lbl.gov

In brief

Eng et al. describe how large omics datasets and computational modeling can guide microbial strain design for highly efficient bioprocesses using renewable carbon streams. These methods are applicable to challenges with other microbes, carbon streams, and bioproducts.

Eng et al., 2023, Cell Reports *42*, 113087
September 26, 2023 © 2023 The Authors.
https://doi.org/10.1016/j.celrep.2023.113087

CellPress

Cell Reports

CellPress
OPEN ACCESS

Article

Maximizing microbial bioproduction from sustainable carbon sources using iterative systems engineering

Thomas Eng,[1,2,13] Deepanwita Banerjee,[1,2,13] Javier Menasalvas,[1,2] Yan Chen,[1,2] Jennifer Gin,[1,2] Hemant Choudhary,[1,3] Edward Baidoo,[1,2] Jian Hua Chen,[4,5] Axel Ekman,[4,5] Ramu Kakumanu,[1,2] Yuzhong Liu Diercks,[1,2] Alex Codik,[2] Carolyn Larabell,[4,5,6] John Gladden,[1,3] Blake A. Simmons,[1,2] Jay D. Keasling,[1,2,8,9,10,11,12] Christopher J. Petzold,[1,2] and Aindrila Mukhopadhyay[1,2,7,14,*]

[1]The Joint BioEnergy Institute, Lawrence Berkeley National Laboratory, Emeryville, CA 94608, USA
[2]Biological Systems and Engineering Division, Lawrence Berkeley National Laboratory, Berkeley, CA 94720, USA
[3]Biomanufacturing and Biomaterials Department, Sandia National Laboratories, Livermore, CA, USA
[4]Department of Anatomy, University of California, San Francisco, San Francisco, CA, USA
[5]National Center for X-ray Tomography, Lawrence Berkeley National Laboratory, Berkeley, CA, USA
[6]Molecular Biophysics and Integrated Bioimaging Division, Lawrence Berkeley National Laboratory, Berkeley, CA, USA
[7]Environmental Genomics and Systems Biology Division, Lawrence Berkeley National Laboratory, Berkeley, CA 94720, USA
[8]QB3 Institute, University of California, Berkeley, 5885 Hollis Street, 4th Floor, Emeryville, CA 94608, USA
[9]Department of Chemical & Biomolecular Engineering, University of California, Berkeley, Berkeley, CA 94720, USA
[10]Department of Bioengineering, University of California, Berkeley, Berkeley, CA 94720, USA
[11]Novo Nordisk Foundation Center for Biosustainability, Technical University Denmark, 2970 Horsholm, Denmark
[12]Synthetic Biochemistry Center, Institute for Synthetic Biology, Shenzhen Institutes for Advanced Technologies, Shenzhen, China
[13]These authors contributed equally
[14]Lead contact
*Correspondence: amukhopadhyay@lbl.gov
https://doi.org/10.1016/j.celrep.2023.113087

SUMMARY

Maximizing the production of heterologous biomolecules is a complex problem that can be addressed with a systems-level understanding of cellular metabolism and regulation. Specifically, growth-coupling approaches can increase product titers and yields and also enhance production rates. However, implementing these methods for non-canonical carbon streams is challenging due to gaps in metabolic models. Over four design-build-test-learn cycles, we rewire *Pseudomonas putida* KT2440 for growth-coupled production of indigoidine from *para*-coumarate. We explore 4,114 potential growth-coupling solutions and refine one design through laboratory evolution and ensemble data-driven methods. The final growth-coupled strain produces 7.3 g/L indigoidine at 77% maximum theoretical yield in *para*-coumarate minimal medium. The iterative use of growth-coupling designs and functional genomics with experimental validation was highly effective and agnostic to specific hosts, carbon streams, and final products and thus generalizable across many systems.

INTRODUCTION

Microbial genomes encode an underexplored reservoir of natural products that have applications in health and biomanufacturing.[1–4] While proof-of-concept quantities of many compounds can be expressed in genetically tractable hosts, scaling up their titers, rates, and yields to appreciable levels is crucial for deployment at commercial scales.[5,6] The economic viability hinges on both the value of the final product and the cost of producing the compound.[7,8] Next-generation strain design approaches should increase the titers, rates, and yields of a targeted final product and also provide scale-up-ready platforms from diverse carbon streams.

To enhance sustainability, replacing common feedstocks like glucose with renewable alternatives such as plant biomass is imperative.[9] Renewable streams also provide the cost savings enabling industrial scaleup and development, based on techno-economic analysis.[10,11] While there are many competing technologies for efficient depolymerization of lignin into its constituent monomers,[12,13] we focus on *para*-coumarate (*p*-CA) as a representative lignin-based carbon stream. Base-catalyzed depolymerization methods have successfully liberated 11%–14% weight of *p*-CA as the dominant monomer from solid lignin-rich residues using different pretreatment regimes and plant biomass.[14,15] Furthermore, plant engineering efforts can increase *p*-CA abundance[16,17] while decreasing lignin recalcitrance.[17]

Soil microbes like *Pseudomonas putida* KT2440 are ideal bioconversion hosts due to their native catabolism of *p*-CA and other lignin-derived substrates.[18,19] Genetic manipulation is facile, resulting in a diverse range of heterologous molecules that have been produced utilizing these non-conventional carbon streams.[20–22] Building upon this foundation, we address the challenge of enhancing final molecule productivity using metabolic models where enzyme activity curation is incomplete. Metabolic models are mathematical representations of steady-state metabolism and are historically informed using ^{13}C-metabolic flux data obtained with positionally labeled isotopes of carbon substrates.[23] While they provide a generalizable and data-driven approach for strain engineering, such data remain scarce for non-canonical carbon sources, partly due to the prohibitively expensive cost of reagents required to conduct flux analysis experiments. Other approaches rely on aromatic carbon flux using mixed carbon sources,[24] but they may not reflect metabolism when grown with aromatics as the sole carbon, which has received recent attention.[25] Rigorously testing alternative methods for model refinement with lignin-derived carbon streams is vital.

Unifying data streams and approaches at a systems level offers a comprehensive understanding of cellular processes and methods for efficient bioconversion. Previous strategies that demonstrate high product titers, though elegant in implementation, remain bespoke.[26–30] We and others have demonstrated systems-level computational strain optimization methods[31–33] using growth coupling, owing to its unique capacity of shifting the production mode from stationary phase to exponential phase to change the product formation rate. Conceptually, growth coupling predicts changes in metabolic models that would force a desired metabolite to be produced as a consequence of growth.[34] This methodology is highly attractive as many products only form in stationary phase including bioplastics, dyes, and potential biofuel molecules.[31,35,36] Our workflow utilizing growth-coupled algorithms is called Product Substrate Pairing (PSP).[31] While some growth-coupling methods are challenging to implement, suggesting upward of >10 gene deletions in a single "cut set" for implementation,[37] we have shown that partial cut sets also improve product rate formation and enable production during growth phase using model substrates.[31] Here we apply the PSP workflow for growth coupling followed by laboratory evolution and systems-level high-throughput omics data analysis to optimize the bioconversion of *p*-CA to a commodity chemical and potential dye, indigoidine.[38,39] This route holds promise for sustainable pigments for use in the circular bioeconomy[40] with lignin-derived aromatics. We achieved the growth-coupled production of indigoidine and exceeded 75% maximum theoretical yield from pure aromatics. Our engineered strains tolerate ionic liquid pretreated and base-catalyzed depolymerized (BCD) sorghum liquor and produce indigoidine, whereas the wild-type (WT) strain cannot.

RESULTS

Implementing PSP workflow for bioconversion of *para*-coumarate to indigoidine

Results from this report correspond to four DBTL (design-build-test-learn) cycles and are indicated in the section titles. In the first cycle, growth-coupled designs for *p*-CA to indigoidine conversion are computed using the PSP workflow. Promising designs are prototyped *in vivo* using multiplex CRISPRi and down-selected for implementation with gene deletions. The second cycle employs adaptive laboratory evolution to enhance growth of the generated triple-deletion strain. Selected isolates undergo further characterization. The third cycle applies rational strain engineering modifications based on this characterization. Last, the fourth cycle refines the genome-scale metabolic model using proteomics data to suggest new deletion targets. These efforts improve indigoidine product titer, rate, and yield in an iterative strain engineering process.

Cycle 1: Selecting a growth-coupled *p*-CA/indigoidine design for implementation

Previously,[31] we described the PSP workflow to assess if a new computational method for growth coupling[37] was feasible in *P. putida* KT2440 using the genome-scale metabolic model (GSMM), iJN1411. The PSP workflow examines output from a growth-coupled algorithm for experimental feasibility (i.e., using RB-TnSeq information)[41,42] and resolves metabolic reactions into specific genes. In turn, these genes are targeted for knockdown with multiplex CRISPR/dCpf1/dCas12a interference (CRISPRi). Since publication of the earlier study, we improved the computational portion. First, we updated the GSMM, iJN1411 to iJN1463, to include additional metabolic reactions. We excluded duplicate reactions and updated the cMCS prediction algorithm to identify genes instead of enzymatic reactions. To account for *P. putida*'s native *p*-CA catabolism to generate biomass and the heterologous indigoidine pathway, we customized the GSMM constraints. We allowed flux through the *p*-CA exchange and the intracellular reactions converting *p*-CA into 3-oxoadipate, which is routed to succinyl-CoA and acetyl-CoA as it enters the TCA cycle. We added the heterologous indigoidine production pathway to the GSMM and predicted the maximum indigoidine production potential in *P. putida* from *p*-CA and other major lignin-derived aromatics. Using the iJN1463, the maximum theoretical yield (MTY) of indigoidine was predicted to be 0.96 g/g of *p*-CA, 0.76 g/g of 4HBA, 0.85 g/g of ferulate, 0.74 g/g of vanillate, and 0.82 g/g of vanillin (Table S1), reflecting subtle differences in aromatic substrate catabolism.

Using the workflow, we assessed the solution space for potential growth-coupling solutions using both the constrained minimal cut set (cMCS) algorithm with the GSMM as well as elementary mode analysis (EMA) with the central metabolic network using a range of minimum biomass and yield constraints (Figures 1A and S1A). The smaller EMA network identified over 2,883 potential elementary modes but suffered from a low (<40% MTY) predicted theoretical indigoidine yield across the analyzed biomass formation rates. In contrast, the cMCS algorithm was computationally time intensive, but out of eight cMCS runs, amounting to over 1,231 cut set solutions, 810 had product yields exceeding 60% MTY (Figure S1B and Table S2). We further down-selected cut sets by stipulating the PSP designs with fewer than 25 genes for intervention and at most one essential gene. Due to the nature of the metabolic networks and cMCS algorithm used, if essential genes are removed from consideration *a priori*, in the majority of cases, zero solutions are returned even after 20 h of computation runtime. Our workaround for this problem was to allow the cMCS algorithm

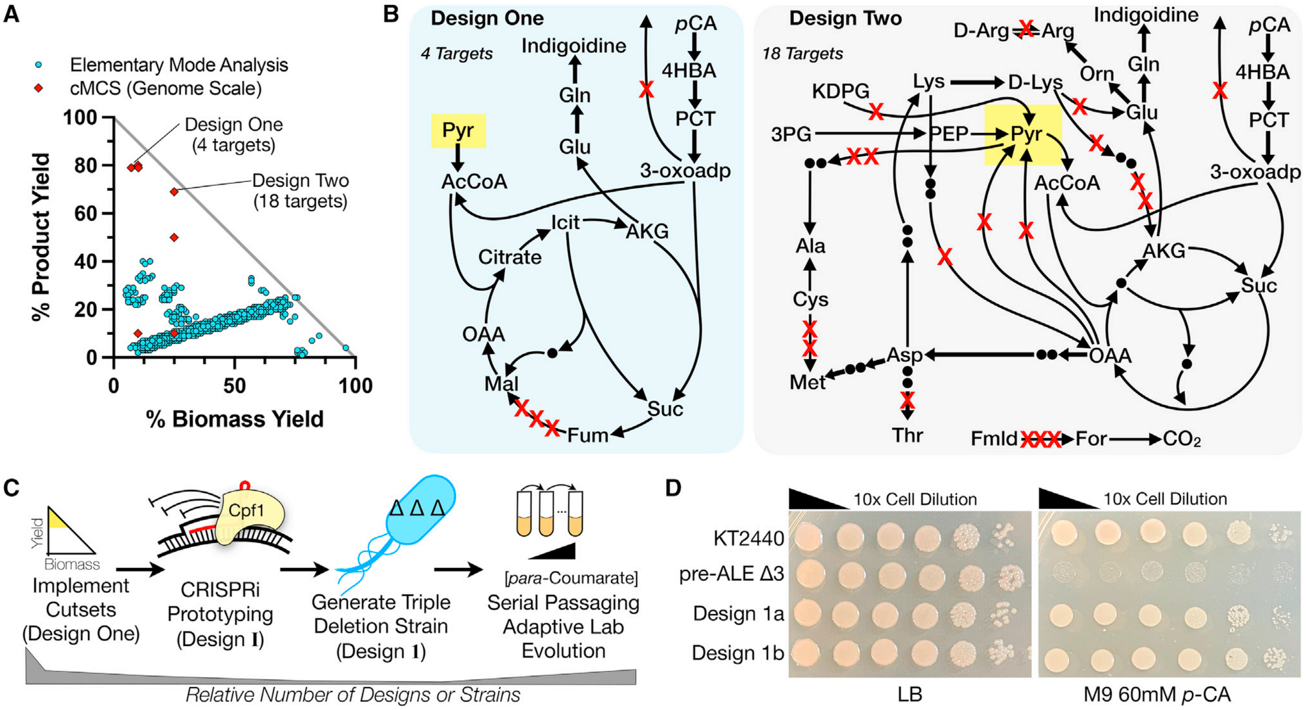

Figure 1. Applying the PSP workflow for the growth-coupled production of indigoidine from *para*-coumarate

(A) Comparison of computational predictions using the constrained minimal cut set (cMCS) vs. the elementary mode analysis (EMA) methods.

(B) Metabolic maps for PSP Designs One and Two selected for implementation. Gene targets are marked with red crosses. In Design One, three isozymes that catalyze the fumarate to malate reaction were targeted. (See Data S2 for gene details.) To aid comparison between metabolic maps of Designs One and Two, pyruvate is highlighted in yellow as a reference point.

(C) Diagram of workflow to compute, prototype, and select *P. putida* strains potentially growth coupled for indigoidine with *p*-CA. The height of the gray bar below indicates the relative number of strains or designs evaluated.

(D) 10-fold serial dilution plating of *P. putida* pre-ALE triple-deletion strain (pre-ALE Δ3) and two post-ALE triple-deletion strain isolates (Design 1a and Design 1b) on LB and M9 60-mM *p*-CA solid agar media. WT *P. putida* (KT2440) is included as a control.

to select essential genes for removal but manually flag them for exclusion after the cut sets were generated.[31] Only two of these designed cut sets with >60% yields conformed to our criteria in the PSP workflow (Table S2) for being experimentally implementable (Figure 1B). Growth-coupled solutions can sometimes generate cut sets that appear intuitive as described in one of the earliest examples, Fong et al.[43] Neither of the computed designs in this work appeared intuitive, i.e., blocking competing reactions for alpha-ketoglutarate limiting glutamine and in turn indigoidine formation. However, both designs empirically enhanced substrate uptake, but inactivating either the TCA cycle in Design 1 or many distal amino acid and formaldehyde pathways in Design 2 appeared unintuitive.

In vitro characterization of inducible and constitutive PSP designs

We evaluated the Design One and Design Two cut sets to identify compatible gRNA sequences for multiplex CRISPRi in *P. putida* harboring an indigoidine expression pathway. By inducing the CRISPRi array, we tested if gene knockdown improved indigoidine production. One of the designs resulted in up to four times improvement in indigoidine yield with subtle growth defects (Figures S1B–S1D), but protein knockdown failed validation by shotgun proteomics (Figure S1E). Nonetheless, this prototyping information was sufficient to select one of these designs over the other for implementation as the multiplex deletion strain.

The Design One solution from the PSP workflow contained four genes for inactivation: three isozymes in the fumarate to malate node (PP_0897, PP_0944, and PP_1755) and a putative alpha-ketoglutarate/beta-keto-adipate permease (*pcaT*/PP_1378). The predicted indigoidine yield from Design One is 76% MTY. PP_0897, annotated as an essential gene, was excluded from this deletion set per our PSP workflow. Our base strain for engineering was the WT *P. putida* KT2440 strain; the heterologous indigoidine pathway was integrated after all deletions were complete. We built this strain (ΔPP_1378 ΔPP_1755 ΔPP_0944; "pre-ALE Δ3" or "Δ3") with CRISPR/Cpf1 aided recombineering (STAR Methods, Figure 1C). The single mutant ΔPP_1378 strain grew slowly on M9 *p*-CA medium but had no discernible defects on Luria-Bertani (LB) (Figure S2A). All double-mutant combinations were viable, but those including ΔPP_1378 were sick on M9 *p*-CA medium (Figure S2A), while the triple mutant ΔPP_1378 ΔPP_1755 ΔPP_0944 strain failed to reliably grow on M9 *p*-CA plates, at most forming pinpoint or abortive colonies after 6 days incubation at 30°C (Figure 1D). These results indicated that the triple mutant exhibited a synthetic lethality to *p*-CA compared to the double mutants. Previously implemented growth-coupled solutions have shown such failure to grow in minimal medium. In such cases, growth could be recovered by nutrient supplementation, indicating a new auxotrophy.[32,33,44]

Cycle 2: Characterization and selection of Design 1 strains by multimodal analysis

We hypothesized that adaptive laboratory evolution[45] (ALE) could allow cells to generate spontaneous bypass mutants that overcome unexpected nutrient auxotrophies. This was implemented by preparing six independent lineages derived from single colonies from independently isolated clones in the Δ3 background as well as several other related strains (see STAR Methods and Figure S2B). We qualitatively monitored indigoidine formation after subsequent serial passages by including the inducer in the growth medium. Tolerant clones that produced indigoidine were recovered in the Δ3 background strain (and in no other derivative backgrounds) and only when the cells were gradually shifted from LB medium without glucose to M9 *p*-CA medium. Curiously, several lineages could not be revived after cryostorage or failed to retain the improved growth in *p*-CA medium phenotype (Figure S2B). These false-positive clones were eliminated from further analysis for the current study. Future studies with additional characterization will reveal the necessary steps required to develop these other strain lineages.

From our tolerization workflow, we isolated spontaneous mutants with improved growth in M9 *p*-CA. These Δ3 isolates from ALE were assigned letter designations and will be referred to as Design 1x or abbreviated as D1x (the arabic number 1 to indicate the deletion strain and the letters a–e to indicate isolate designation). We tested a range of isolates from different time points in the serial passaging regime. As hinted from several earlier studies, there may not be a strong correlation between growth and product titers post ALE for growth-coupled production.[43,46] Strains D1a and D1b were recovered after 18 or 19 serial passages, respectively (Figure 1D), which is equivalent to approximately 90–95 doublings. Since these isolates were selected for growth under increasing concentrations of *p*-CA, we next screened mutants from the archival cryostocks to determine if the gain in *p*-CA tolerance modulated indigoidine production.

Indigoidine titers were measured in the deep-well plate format where our CRISPRi strains had shown high variability in product titers (refer to Figure S1B) at the 24- and 48-h time points post pathway induction (Figure 2A). Many isolates showed comparable titers to the WT control with the exception of D1e, which was a poor producer (Figure 2A). Most strains produced around 1 g/L indigoidine under routine cultivation conditions, but D1e produced less than 100 mg/L indigoidine. We also examined tolerance of these isolates for growth at high concentrations of *p*-CA in M9 medium (Figures 2B and S2C). Strains D1a and D1b had comparable tolerance to WT, growing at 100 mM *p*-CA. The decrease in indigoidine titer correlated with this strain's tolerance against high concentrations of *p*-CA. In contrast, isolate D1e exhibited robust growth at 200 mM *p*-CA and reduced lag times at concentrations equal to or lower than 100 mM *p*-CA, outperforming the control. As there are many reasons strains could have lost indigoidine productivity, such as due

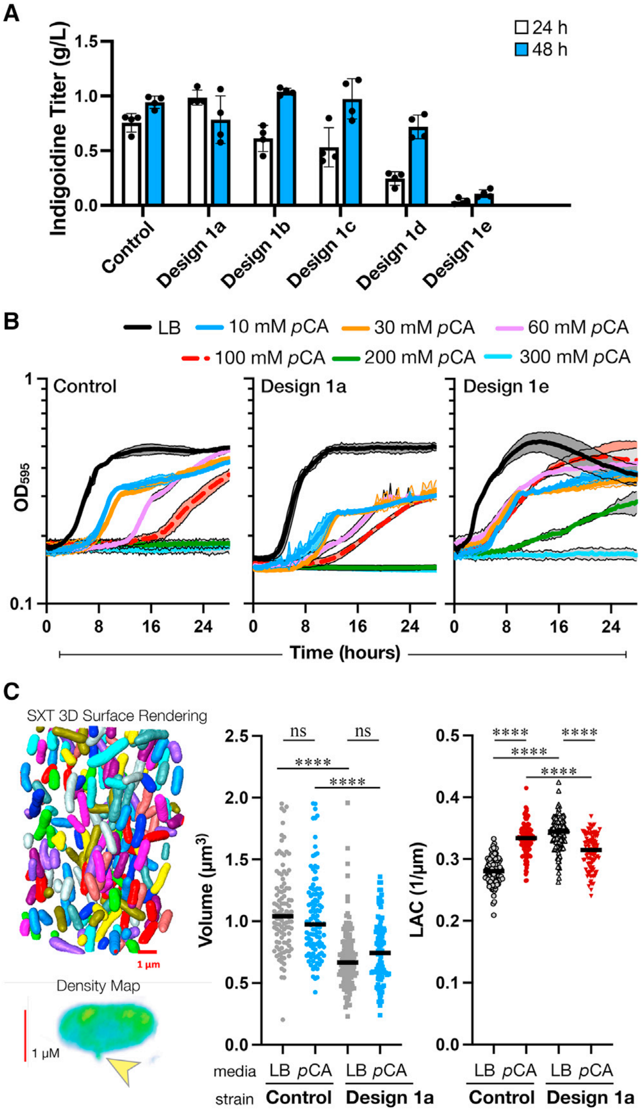

Figure 2. Initial characterization and down-selection of post-ALE Design 1 isolates

(A) Indigoidine production was assayed across post-ALE Design 1 isolates (D1a, D1b, D1c, D1d, D1e) and compared to WT in a 24-well deep-well plate M9 60-mM *p*-CA medium with 0.3% (w/v) arabinose. Indigoidine titer was quantified at the time points indicated. The error bar represents mean ± SD (n = 4).

(B.) Post-ALE Design 1a and Design 1e strains were assayed for growth and tolerance at the *p*-CA concentrations indicated in M9 minimal medium in a microtiter plate. The shaded region between the color bands represents mean ± SD (n = 3). Refer to Figure S4B to normalize OD values from a plate reader to a standard 1-cm cuvette measurement.

(C) Soft X-ray tomography (SXT) analysis of Design 1a and WT strains in LB medium and M9 60-mM *p*-CA and 0.3% (w/v) arabinose. Left, top: 3D surface rendering from SXT. Left, bottom: a high density membrane aberration consistent in appearance with the formation of an outer membrane vesicle (OMV) is highlighted with a yellow arrow. Middle: volumetric quantification. Right: cell density analysis as measured by linear absorption coefficient (LAC). Strains and growth conditions for each sample are indicated on the bottom below the X axis. The solid black line on the graph represents the average value. Ns, not significant. $p < 0.0001$ is represented by ****. At least 99 cells were examined for each dataset.

to inactivating mutations in the heterologous pathway or inducer system, we selected the two best performing clones (D1a and D1b) for both highest absolute indigoidine titer and the best titer at 24 h, as it could reflect a kinetic shift toward growth-coupled production.

Cellular and morphological changes detected in Design 1 isolate

Recent work suggests *p*-CA may be catabolized in outer membrane vesicles (OMVs) that are induced by an unknown lignin component.[47–50] We asked if extracellular metabolite sharing could explain how Design 1 strains restored growth on *p*-CA. To this end, we obtained mesoscale resolution (∼25 nm) of intact cryo-fixed cells without fixatives using soft X-ray tomography[51] (SXT) to detect potential OMVs and other structural changes. SXT also provides quantitative information about the density and composition of organic molecules. This analysis showed structural and morphological differences in composition of the D1a strain compared to the control strain as well as the appearance of dense membrane structures consistent with previous reports of OMVs in the process of budding (Figures 2C and S3A). Membrane-bound buds were approximately 270 nm in size (Figure S3A) and emerged from both WT and strain D1a, matching the reported OMV dimensions.[50] In both LB and M9 *p*-CA media, cells from D1a were volumetrically smaller and had increased density when quantified with the linear absorption coefficient (LAC) (Figure 2C). Strain D1a showed decreased cell density in M9 *p*-CA medium compared to LB medium. In contrast, the control strain showed increased density from LB to M9 *p*-CA medium. While D1a cells are smaller volumetrically, there was no change in cell population density as measured by serial dilution plating, absorbance at optical density 600 (OD_{600}), or quantitative colony formation unit (CFU) plating analysis (Figures S2D and S3A). Changes in cell density have been previously reported correlating with cell-cycle progression in mitotically synchronized fission yeast cells, but the biological relevance related to restoring *p*-CA catabolism is unclear.[52] From this physical characterization, we conclude that the changes in *p*-CA tolerance and the resulting restoration of indigoidine production have generated persistent changes in cell shape and density that are apparent under rich medium cultivation conditions, and that nascent OMVs can be detected in cells frozen in their near-native states without crosslinking reagents.

Diffusible molecules that are exchanged between adjacent strains on an agar plate are detectable if they change the growth patterns of the proximal microbe.[53] We tested if any metabolite exchange occurred using a Δ*fcs* strain (deficient in the first step of *p*-CA catabolism) to measure if this Δ*fcs* strain could access *p*-CA-derived metabolites generated from adjacent WT cells on an agar plate. The Δ*fcs* strain did not show robust growth when placed adjacent to the WT or strain D1b in this interaction assay (Figures S3B and S3C), which is consistent with a similar liquid culture report measuring OD changes from Salvachua et al.[50]

Whole-genome sequencing analysis

Next we characterized the genetic changes in these strains using hybrid *de novo* genome assembly (Figure 3A and STAR Methods). Reads were assembled into contigs (STAR Methods, Figure S2E), and polymorphisms were analyzed for correlations with restored growth on *p*-CA (STAR Methods).

Three mutations in the Design 1 strains warrant attention. First, unique point mutations in the upstream promoter of PP_1378 were identified, a gene we targeted for deletion. Strain D1a contained a G/A substitution at the −6 position, and strain D1b contained a C/G substitution at the −12 position. Removing PP_1378 may have impacted expression of the remaining genes in the PP_1378-PP_1381 (*pcaTBDC*) operon even though the upstream promoter sequences were intact. This operon is crucial to the conversion of intermediate metabolites 4-hydroxybenzoate (4-HBA) to protocatechuate (PCT) in the *p*-CA catabolism pathway. The ΔPP_1378 single-mutant strain grows poorly in M9 *p*-CA medium (Figure S2A), consistent with the need to accumulate an activating mutation in this *pcaTBDC* promoter region. Second, we detect gain of function mutations in two transcriptional regulators PP_3493 and PP_4338. RB-TnSeq analysis[41] indicates their inactivation leads to weak fitness defects on different aromatics but not glucose (STAR Methods); it is possible the mutants here increase their activity. The PP_3493-N215S mutation impacts the protein substrate recognition domain, while PP_4338-N72S impacts the phosphotransferase domain of a chemotaxis-related histidine kinase, which could modulate the activity of this signaling cascade. *P. putida* is known to induce chemotaxis toward aromatic molecules with some cross-activation of their cognate catabolic pathways.[54] These mutations, one in *p*-CA catabolism and two transcriptional regulators, are the most likely genes implicated in restoring growth on *p*-CA in these two isolates by DNA resequencing.

Characterization of Design 1 strains using shotgun proteomics

Shotgun proteomic analysis enabled a quantitative characterization of ∼2,100 unique proteins in the Design 1 strains and provided insights into metabolic rewiring. The key finding from the proteomics analysis was the identification of a new route for how carbon was rewired from *p*-CA to indigoidine. The fumarate to malate node was bypassed by increasing proteins needed for the glyoxylate shunt pathway, redirecting flux from lysine toward AKG, and in turn favoring glutamine and indigoidine formation.

In the Design 1 strains, we detected 123 metabolic and 206 non-metabolic proteins with differential protein counts compared to the control (Figure 3B). While there were clear correlations of upregulated aromatic catabolic pathway proteins known to have fitness defects across all aromatic molecules profiled by RB-TnSeq (STAR Methods), there was no correlation between the differential protein changes for TCA cycle, glycolytic, homogentisate, or metal cofactor proteins profiled.

To assess changes in *p*-CA catabolism, we compared all double mutant pairs with the Design 1b strain using proteomics. Both double-deletion strains lacking PP_1378 had reduced counts (between 2- and 8-fold $\log_2$) for the proteins responsible for converting 4-HBA to PCT in *p*-CA catabolism (Figures S4A and S4B). This is consistent with their slow growth phenotype on M9 *p*-CA medium (Figure S2A). In contrast, the ΔPP_1755 ΔPP_0944 strain expressed higher levels of PcaB than strain D1b, with no growth defect on M9 *p*-CA. The restored growth

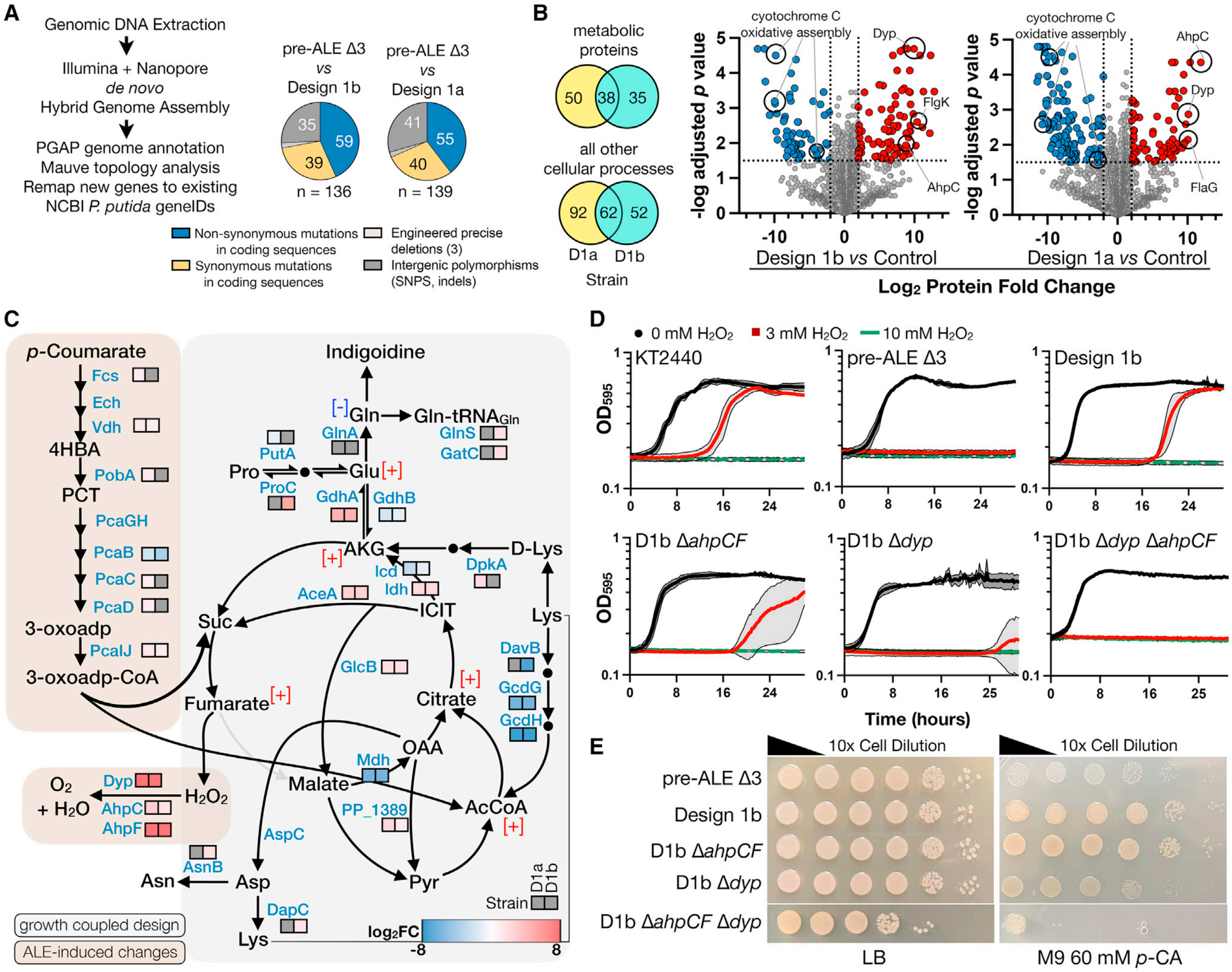

Figure 3. Multi-omics analysis of PSP Design 1 clones a and b

(A) Left: hybrid genome assembly and annotation workflow. Right: pie charts comparing pre-existing mutations in the pre-ALE Δ3 strain to the two post-ALE isolates, Design 1a (D1a) and Design 1b (D1b) clones.

(B) Left: Venn diagram of significantly enriched proteins for D1a and D1b. Right: ~2,200 proteins detected by LC-MS/MS of D1b and D1a compared to the control strain.

(C) Proteomics analysis of inferred changes in central metabolism due to ALE (brown box) or Design 1-based gene deletions (gray box). Key metabolites in a D1b derivative strain were quantified by LC-MS, and metabolite concentrations higher than 2-fold are indicated with [+] in red; and reduced by 5-fold is indicated with [–] in blue. (Refer to Figure S4 for double-deletion strains).

(D) Top: peroxide sensitivity of WT *P. putida*, pre-ALE Δ3, and D1b isolates to exogenous hydrogen peroxide (H_2O_2) in a kinetic growth assay. Concentrations of hydrogen peroxide in LB medium were 0 mM, 3 mM, and 10 mM. Bottom: single- and double-deletion mutants lacking peroxidase encoding genes *ahpCF* and/or *dyp* in the D1b background were also tested. The shaded region between the solid line indicates mean ± SD (n = 3).

(E) 10-fold serial dilution of *P. putida* peroxidase mutant strains in D1b background on LB or M9 60-mM *p*-CA plates. The pre-ALE Δ3 strain is included for comparison.

and protein levels in the Design 1 strains correlate with the unique point mutations recovered in the promoter sequence upstream of PP_1378 described for strains D1a and D1b. The decrease in pathway protein abundance for several other steps in the conversion of 4-HBA to PCT suggests the loss of *pcaTBDC* operon expression impacted other pathway proteins including PobA, PcaIJ, and PcaGH. We conclude that the Design 1 strains restored conversion of *p*-CA into 3-oxoadipyl-CoA as a consequence of ALE.

The data also suggested there was an active shunt of the carbon flux toward succinate and malate to bypass the inactive part of TCA due to the targeted gene deletions (Figure 3C). Examining the Design 1a and 1b strains vs. WT control dataset, we observed differences in the conversion of fumarate to malate. PP_0944 protein counts were reduced below the detection limit consistent with its expected gene deletion. PP_0897, the third fumarate to malate isozyme, had 25%–30% higher protein counts in both D1 isolates than WT. At the malate to oxaloacetate node, malate dehydrogenase (Mdh/PP_0654) had zero protein counts; Mqo3 protein had a significant fold reduction (only 9%–26% that of WT), whereas the other two quinone-dependent malate oxidoreductase proteins, Mqo1 and Mqo2, were slightly elevated in strains D1a and D1b compared to WT. This implies that malate is rerouted into pyruvate (MaeB/PP_5085, nearly 2-fold higher protein abundance). 3-oxo-adipyl-CoA can also enter the TCA cycle through acetyl-CoA catalyzed by GltA. We detected increased protein counts in both D1 isolates strains compared to WT. Citrate to isocitrate proteins AcnA1, AcnA2, and AcnB had similar or higher protein counts in both D1 isolates compared to WT with the exception of AcnA1 in strain D1a (reduced to 10% of WT). The isocitrate to alpha-ketoglutarate (AKG) metabolic step uses the isocitrate dehydrogenase isoforms Idh/PP_4012 and Icd/PP_4011. Idh was upregulated, while Icd was downregulated. AlphaFill analysis[55] indicated differences in protein enrichment might be due to differential NADH/NADPH cofactor specificity (Data S1). Isocitrate through the glyoxylate shunt via AceA/PP_4116 was upregulated (>2.59), and GlcB (>1.57) also had 3-fold higher protein counts. Proteins involved in AKG to succinyl-CoA (SucA, SucB, and LpdG) were reduced by 20%–50% of protein counts compared to WT. Overall, all the proteins involved in TCA were similar or higher than WT protein counts except for the expected deleted genes and Mdh/PP_0654.

Finally, several proteins related to the downstream metabolite pools needed for indigoidine formation were upregulated in the rewired strain. Indigoidine is derived from the condensation of two glutamine molecules, which are generated from glutamate and in turn AKG. Glutamate dehydrogenase GdhA/PP_0675 (>4.61), was highly upregulated in both D1 isolates, while GdhB/PP_2080 (<–1.42) was downregulated. Glutamine synthetases, GlnA and PP_4399, had decreased protein counts to 50%–60% in D1a and 8%–30% in D1b of WT levels. Lysine reentry into the TCA cycle via the AKG node was favored over acetyl-CoA. DpkA/PP_3591 was highly enriched in the Design 1 strains, with raw protein counts higher than 2.79-fold compared to WT, whereas lysine metabolism toward acetyl-CoA via glutarate metabolic proteins DavB/PP_0383, GcdH/PP_0158, and GcdG/PP_0159 was significantly reduced or undetected in both the D1 isolates. Glutamate metabolism toward glutathione biosynthesis through protein GshA was 4-fold higher than the WT control. Levels of glutathione are important in maintaining redox balance and are closely linked to oxidative stress responses in *P. putida*.[56] These changes in lysine metabolism are unexpected and indicate how the unintuitive deletions suggested from the computational predictions have implications for other aspects of cell physiology and metabolism.

The relative metabolite concentrations agreed with the implied changes from the proteomics analysis (Data S2). Reduced flux through the fumarate to malate node was confirmed with a 2.7-fold increase in fumarate concentration in strain D1b compared to WT. Acetyl-CoA and citrate had increased by 2-fold, while AKG had increased by 2.71-fold. Finally, glutamate had increased by 4.4-fold and glutamine decreased by 6-fold. This D1b derivative strain expresses an additional copy of *glnA*. These metabolite concentrations provide important evidence corroborating the differential protein expression as a proxy for metabolism we have observed in these Design 1 strains.

Upregulated peroxidases are necessary to remedy oxidative stress in Design 1 strains

The upregulated oxidative stress proteins suggested a mechanism for restored growth in the Design 1 strains. Two types of peroxidases (Dyp/PP_3248; AhpCF/PP_2439, PP_2440) were highly upregulated in both strains D1a and b (Figures 3B and S4B). Peroxidases catalyze the reduction of hydrogen peroxide (H_2O_2) to water and oxygen or organic peroxides to water and alcohols.[57] Design 1 strains accumulate fumarate due to the deletion of two key enzymes that convert fumarate to malate (Figure 3C, Data S2). Fumarate reductase is a major source of hydrogen peroxide, and in *E. coli* the AhpC homolog is known to ameliorate these peroxides during aerobic growth.[58–62] We hypothesized growth on *p*-CA medium generates additional reactive oxygen species normally remedied via the electron transport chain reaction; we tested this hypothesis by interrogating if these pre- and post-ALE strains were differentially sensitive to H_2O_2. Deleting the peroxidases would resensitize the strains to peroxides as well as block growth with *p*-CA as the sole carbon source.

Using an exogenous peroxide stress assay (STAR Methods), we observed that WT *P. putida* strains were able to grow in the presence of 3 mM H_2O_2, but the pre-ALE Δ3 strain failed to grow in the presence of this environmental stressor (Figure 3D). As controls, the single mutants ΔPP_1755 and ΔPP_1378 or the ΔPP_1755 ΔPP_1378 double-mutant strain were not sensitive to 3 mM H_2O_2 (Figure S4C). Importantly, growth was restored with 3 mM H_2O_2 in the Design 1b strain. Next, deleting either of the peroxidases (*ahpCF* or *dyp*) in the Design 1b strain impaired growth in peroxide-containing media; deleting both peroxidases in the D1b strain reduced growth to the same background level as the pre-ALE strain. The D1b Δ*ahpCF* strain did not show any growth defect on M9 *p*-CA plates, but D1b Δ*dyp* strain showed a pronounced growth defect that formed pinpoint colonies after 3 days (Figure 3E). The double-mutant strain, D1b Δ*ahpCF* Δ*dyp*, failed to grow on M9 *p*-CA medium, only forming colonies on the first spotted dilution with no background growth at higher dilutions, confirming our hypothesis. Overexpression of the *dyp* peroxidase was insufficient to confer growth in the pre-ALE Design 1 strain, consistent with our model where additional compensatory mutations are necessary for restoration of growth (Figure S4D). These results indicate that the growth-coupled design needed tolerance toward additional reactive oxygen species generated as a consequence of the rewired metabolism and that upregulating both peroxidases was necessary to restore growth on *p*-CA.

In summary, the multimodal analysis identified a suite of morphological, genetic, and functional changes characterizing Design 1 isolates from this DBTL cycle. The accumulation of several mutations in the *pcaTBDC* operon suggested gene expression for *p*-CA catabolism was suboptimal after deletion of *pcaT*. However, even with restored substrate catabolism, the computed Design could not account for the increase in oxidative stress, necessitating the upregulation of peroxidases for growth on higher concentrations of *p*-CA from the ALE serial passaging regime. With these two deficiencies remedied, the partial inactivation of the fumarate to malate node routed flux through the TCA shunt, revealing the growth-coupled formation of indigoidine described in the next section.

Cycle 3: Increasing growth-coupled indigoidine production with rational engineering methods

We next interrogated the relationship between growth and indigoidine final product yield in our Design 1 strains. The basic parameters for cultivation and product characterization were established by generating a new indigoidine standard curve produced from WT *P. putida* KT2440 expressing the heterologous indigoidine pathway (control strain) from *p*-CA (see STAR Methods and Figures S5A and S5B). Cultivation medium parameters were also evaluated; a range of starting *p*-CA concentrations of 60–120 mM *p*-CA was optimal when either ammonium sulfate or ammonium chloride was used as the nitrogen source, and 100 mM ammonium ion concentration yielded slightly improved titers of 1 g/L indigoidine with tighter confidence intervals (Figure S5C). The major difference in culture media between the initial production data shown in Figure 2 with the optimized condition was a switch from 15 mM ammonium sulfate to 100 mM ammonium chloride. We also developed an orthogonal liquid chromatography-mass spectrometry (LC-MS)-based method to quantify indigoidine (Figure S5D). Purified indigoidine does not contain any detected contaminants as the quantification from the colorimetric assay strongly correlates with the reported values from LC-MS analysis ($R^2 = 0.9984$) (Figure S5D).

The desired outcome for a growth-coupled strategy is shifting the production phase to the exponential growth phase. To interrogate if indigoidine became growth coupled when fed *p*-CA in the Design 1 strains, we prepared samples for a time course analysis to characterize production during exponential growth. Indigoidine yields from both Design 1 strains were compared to the control *P. putida* production strain. While strain D1a and D1b produced indigoidine at the 8-h time point (7 mg indigoidine/g *p*-CA and 75 mg indigoidine/*p*-CA, respectively), WT control strain did not (Figure 4A, left panel). We confirmed that at the 5- and 8-h time points, all three strains were still consuming *p*-CA until the 24-h time point (Figure 4A, right panel). We note that the control strain at this same mid-log time point had 5-fold more Sfp indigoidine pathway protein expression than Design 1b, indicating that pathway protein expression alone is insufficient to drive indigoidine formation during the growth phase (Data S2). The shifting of indigoidine from stationary phase to log phase production extends our initial observation from glucose[31] to an aromatic carbon stream.

While Design 1 strains here improved the overall rate, they did not meaningfully increase the final product titer (refer to Figure 2). We addressed this by taking a rational strain engineering approach by examining precursor supply, as glutamine synthetase protein counts were somewhat reduced in the Design 1 strains (Figure 3C). We augmented the indigoidine production pathway by introducing the glutamine synthetase *glnA* from either *P. stutzeri* RCH2 or *P. putida* KT2440 downstream of the existing pathway to form a three-gene operon under the control of the BAD promoter. The introduction of *glnA* from *P. stutzeri* RCH2 showed a robust improvement to indigoidine titer in both Design 1 strains, increasing titers up to 2-fold to 2 g/L and therefore was chosen for subsequent strain engineering (Figure S5E). The same three-gene indigoidine pathway had limited improvement on titer when expressed in the control strain (Figure S5E), suggesting GlnA activity was only rate limiting in the Design 1 isolates. Next, we varied the arabinose inducer concentration, and we observed that higher indigoidine titers were possible by increasing the concentration from 0.3% to 1.5% arabinose, but here, we only observed an improvement in the control strain and not the Design 1b strain (Figure S5E).

The proteomics dataset provided additional targets for greater improvements to indigoidine titer. Both Design 1 strains showed many flagella-related proteins were upregulated $\log_2$ 4- to 10-fold over the control. In *P. putida*, approximately 8% of energy in a cell is devoted toward cell motility and is controlled by the FleQ transcriptional master regulator.[63,64] We tested indigoidine production in Design 1b *glnA* strain after deleting *fleQ* and found that titers increased from 2 g/L to ~5 g/L in this new strain (Figure 4B). The titer values from the deep-well plate were corroborated by LC-MS. The control KT2440 Δ*fleQ* strain in comparison only showed a 30% indigoidine titer improvement, likely reflecting the increased flagella-based metabolic burden in the Design 1 strains (Figures 3B and S5E). The D1b *glnA* Δ*fleQ* strain showed stable indigoidine titers across cultivation formats in both the deep-well plate and shake flask formats with similar titers at 5.1 g/L at the 48-h time point (Figures 4B and 4C). In shake flasks, a decreased total fill volume led to higher early titers (200 mg/L) compared to the original D1b strain at the 8-h time point (Figure 4A). The strains used in Figure 4C in the 20-mL shake flask setup were analyzed for metabolite concentrations that were described earlier in Figure 3C. These results indicate the robustness of *p*-CA to indigoidine bioconversion in the Design 1b *glnA* Δ*fleQ* strain under different cultivation formats.

Finally, we used strain D1b *glnA* Δ*fleQ* to produce indigoidine from real-world lignin-derived carbon streams by replacing commercially purchased *p*-CA with sorghum biomass-generated BCD liquor (STAR Methods). The concentration of *p*-CA present in 1x M9 BCD liquor medium was ~138 mg/L, which is suboptimal for indigoidine production based on our previous work in C/N ratio (Figure S5C). Furthermore, there are many other characterized aromatic molecules present in BCD liquor that might also be co-catabolized with *p*-CA, which may or may not be compatible carbon substrates for the initial growth-coupled design (Table S1). While both the control strain and the D1b *glnA* Δ*fleQ* strain were able to grow in M9 BCD liquor, strain D1b *glnA* Δ*fleQ* was able to reach somewhat higher densities at the 24-h time point by serial dilution of cultures spotted onto LB agar medium (Figure S5F). Importantly, we observed in this batch of M9 BCD liquor, only the D1b *glnA* Δ*fleQ* strain was able to produce 500 mg/L indigoidine within 24 h, while the control strain did not produce detectable indigoidine even after 48 h (Figure 4D). This result suggests the D1b *glnA* Δ*fleQ* strain was more tolerant of BCD liquor containing a mixture of carbon streams for indigoidine production, whereas the control strain failed to produce any indigoidine with this batch of sorghum BCD liquor. As this yield exceeds the initial *p*-CA concentration in M9 BCD liquor, we presume that other carbon sources present in BCD liquor were used to generate this quantity of indigoidine.

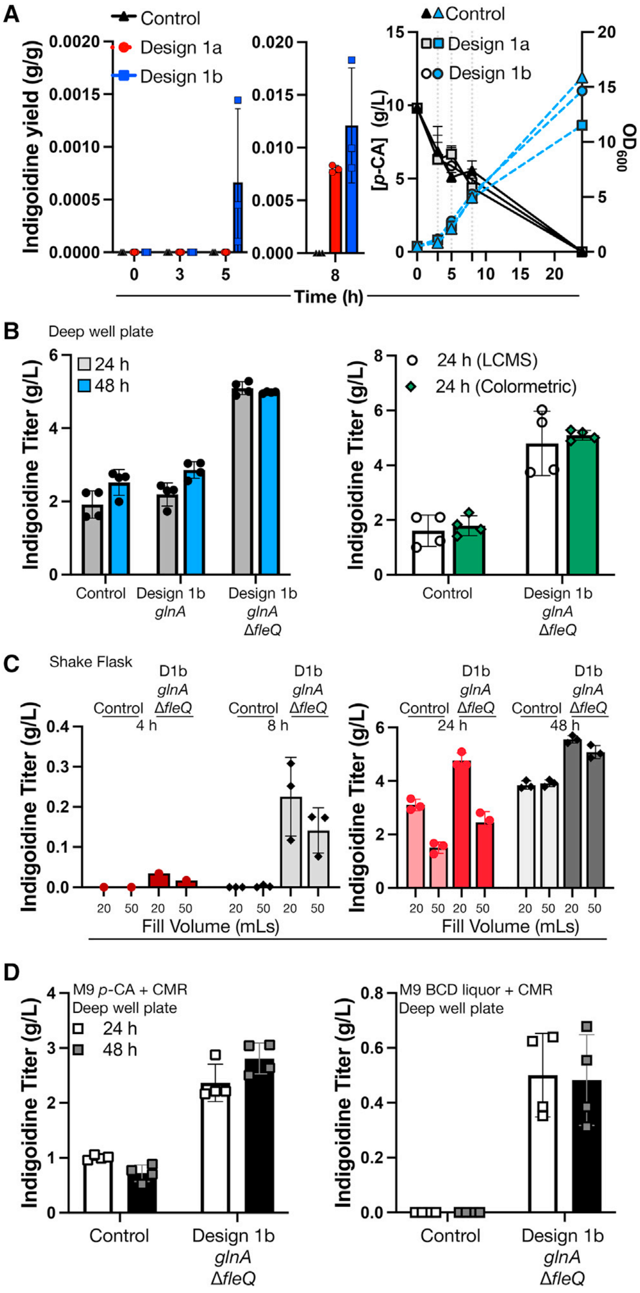

Figure 4. Demonstration of growth-coupled bioconversion of *p*-CA to indigoidine and rational strain engineering approaches to increase titers

(A) Indigoidine production kinetics in shake flasks with 0.3% w/v arabinose. The indigoidine yield was calculated as grams per gram (g/g) of *p*-CA consumed at the given time point.

(B) Left: indigoidine assay for Design 1b augmented with *P. stutzeri glnA* and deletion of *fleQ,* the master regulator of the flagella biosystem. Arabinose inducer concentration was increased from 0.3% to 1.5% w/v. Right: titers from the colorimetric method were cross-validated using LC-MS.

(C) Indigoidine production kinetics of Design 1b *glnA* Δ*fleQ* compared to WT, as in (A) at the time points indicated in 20 mL and 50 mL fill volumes in 250-mL shake flasks. Arabinose was used at 1.5% w/v.

(D) Indigoidine production for *P. putida* control strain harboring the indigoidine production pathway and the Design 1b *glnA* Δ*fleQ* strain using base-catalyzed depolymerization (BCD) sorghum liquor. Arabinose was used at 1.5% w/v. (See Table S1 for aromatic carbon composition of BCD liquor.) Error bars represent mean ± SD (n = 3) in (A) and (C) and mean ± SD (n = 4) in (B) and (D).

Cycle 4: Refining genome-scale metabolic model constraints with proteomics

To fully utilize all information generated from the proteomics data, we adapted an existing workflow for integrating transcriptomics or proteomics data into GSMMs. Using the iMAT algorithm,[65] we integrated the GSMM with proteomics data that generated a flux activity state for each reaction in the model, re-constraining the presence or absence of the metabolic reaction annotated in the GSMM for the WT strain. We generated two context-specific models representing strain D1a (iMATD1a559) and strain D1b (iMATD1b539) (Figure 5A). The resulting iMATD1b539 model reduces the active 1,644 reactions in the original GSMM under *p*-CA minimal medium condition to 558 reactions. This model contains 558 reactions, 543 metabolites, and 539 associated genes. We also considered using proteomics data from strain D1b *glnA* Δ*fleQ,* but the flagellar master regulator does not regulate many metabolic processes based on our analysis (Data S2). Satisfied that the Δ*fleQ* deletion would not change the differential protein counts used for constraints, we used the iMATD1b539 model to compute a second PSP cycle for growth-coupled production of indigoidine from *p*-CA. We computed cut sets using a minimum of 80% MTY of indigoidine and a maximum of 25% MTY biomass yield. This resulted in the smallest cut set with a total of four metabolic genes: PP_4120, PP_0158, PP_0597, and PP_0253. PP_0253 was excluded as it is a pseudogene, and we note that ΔPP_4120 was previously identified as a deletion that can both improve indigoidine titer and strain fitness in a bioreactor.[66] As before, we sequentially generated and tested the next three deletions in the D1b *glnA* Δ*fleQ* strain for indigoidine production. While the new strains containing one additional deletion did not show appreciable titer increases, strain D1b *glnA* Δ*fleQ* PP_4120 ΔPP_0158 increased titers from 4.5 g/L indigoidine to 6.2 g/L, equivalent to 65.6% MTY (Figure 5B). The completed cut set strain D1b *glnA* Δ*fleQ* ⊿PP_4120 ΔPP_0158 ΔPP_0597 further increased indigoidine titers to 7.3 g/L, equivalent to 77% of the MTY from *p*-CA (Figure 5B). Unlike the previous iteration Design 1b isolates, we now observe a growth defect in this strain with smaller colonies and fewer absolute number of CFUs on M9 *p*-CA plates as well as slower growth in liquid cultures (Figures 5B and S5G), suggesting a trade-off between high indigoidine titers and biomass formation.

DISCUSSION

GSMMs are comprehensive representations of cellular metabolism that have potential in the predictive design of microbes. GSMMs have been extended to heterologous pathways and many other organisms.[34,67] These methods are ideal for optimizing bioconversion processes to produce commodity chemicals as most require high productivity using a range of carbon sources. Designing microbes for this purpose is nontrivial, and the execution is rarely predictable.

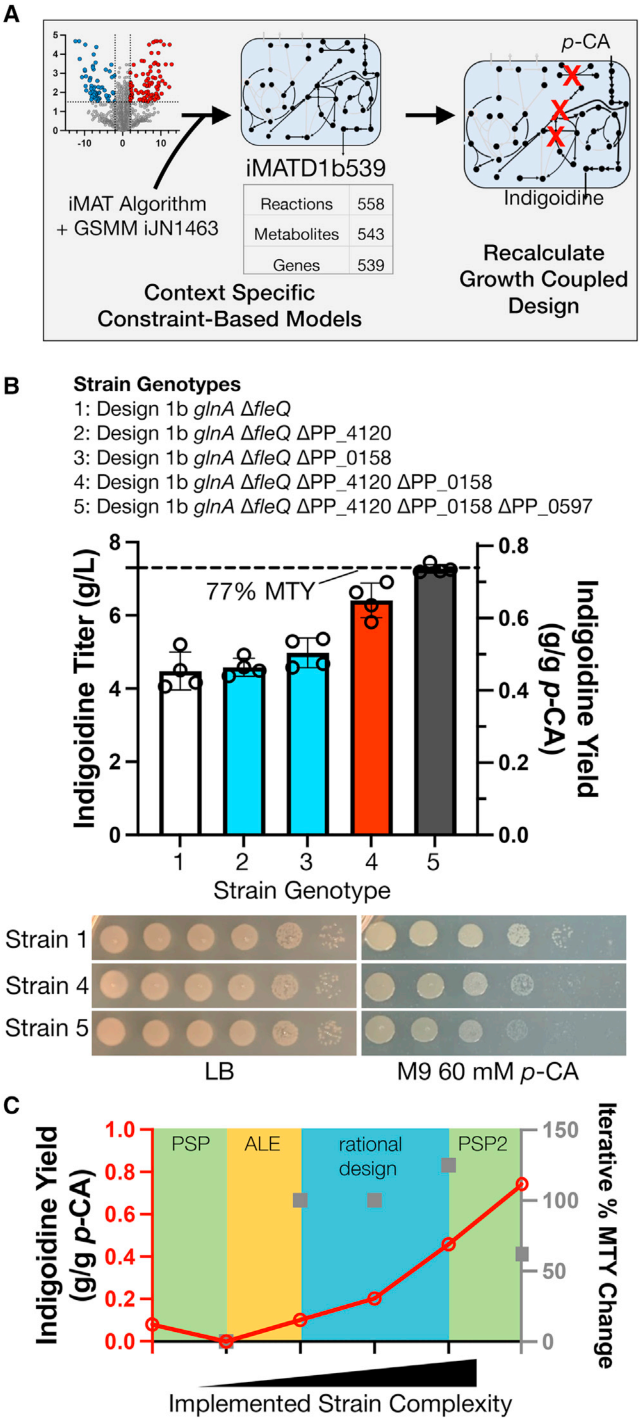

Figure 5. Context-specific models using proteomics constraints led to maximal indigoidine titers

(A) Model-based proteomics data integration pipeline. In a second PSP cycle (PSP2), we recomputed gene deletion targets for the growth-coupled production of indigoidine from *para*-coumarate using a new proteomics-informed, context-specific metabolic model (iMATD1b539).

(B) Indigoidine production profile (top) and 10-fold serial dilution plating assay (bottom) for *P. putida* strains generated from the second cycle of PSP. Samples were grown in deep-well plates and analyzed for indigoidine production from the 24-h time point. 1.5% w/v arabinose was used as the inducer. The strain genotypes assayed are indicated in the figure. The error bars represent mean ± SD (n = 4).

(C) Summary of cumulative indigoidine yield gains (solid red line) and iterative percent MTY change for each subsequent strain generated (gray squares, ■). The color blocks indicate the method of strain engineering used in each DBTL cycle. PSP, best multiplex CRISPRi prototype and initial triple deletion strain; ALE, post ALE Design 1 isolates, highest titer; rational design, C/N ratio optimization, integration of *P. stutzeri glnA*, and deletion of *fleQ*; PSP2, three additional deletions based on the second cycle of PSP (PSP2) using iMATD1b539.

Here we implemented growth coupling for both the expression of a heterologous product and the use of a non-canonical carbon source. From our previous work,[66] we anticipated that many important non-metabolic processes would impact final product titers but were unaccounted for in the GSMM. We affirm that the current state of the *P. putida* GSMM and tools for growth coupling are well poised for effective strain engineering. Applications where metabolic flux information (and model confidence) is limited can be remedied with these methods to produce final products distal from their starting substrates. The initial objective of reaching a 76% MTY indigoidine from *p*-CA was achievable with 10 rounds of modifications: six deletions predicted across two rounds of the PSP workflow, three targets from rational strain design, and ALE. This iterative workflow described here (Figure 5C) can be easily applied to other processes by building upon improvements achieved from different methodologies. Furthermore, optimization algorithms that can suggest both gene deletion and overexpression[68] or use kinetic modeling[69] can extend this method to search a larger solution space.

With a highly curated model or strong mechanistic understanding, predictions can be translated into complex strain designs. Here, the three pillars of this workflow—CRISPR, GSMMs, and proteomics—are increasingly available for many non-model microbes. Our previous study on growth coupling with glucose using multiplex CRISPRi led to ~45% indigoidine MTY without the need for ALE.[31] However, for *p*-CA growth-coupling sets, we encountered many technical issues limiting a direct implementation of GSMM predictions. ALE has been long recognized for its potential to generate gain-of-function mutations relevant for growth coupling,[43] especially in the context of substrate catabolism.[70–72] Our predictions initially indicated considerable growth defects in these strains (Figure 1A), and ALE in conjunction with PSP provided strains with comparable growth and indigoidine titers to the WT control. Even partial growth-coupled designs may impose an equally challenging (and distinct) evolutionary landscape, owing to the challenges posed when key metabolic pathways are removed. The gain of function mutants identified by whole-genome sequencing likely reflect the evolutionary path[73] our base strain navigated to restore growth on *p*-CA, in contrast to WT *P. putida* used previously.[74] The role of cell shape and structure as well as the underlying molecular mechanisms for their applicability to strain engineering are only beginning to come into focus.[75]

The utility of proteomics datasets to build a process understanding cannot be overstated. Proteomics analysis identified oxidative stress as a key cause of inviability in the pre-ALE Δ3 strain, which was alleviated by the upregulation of the Dyp and AhpCF peroxidases in the Design 1 isolates. It also identified FleQ, a master regulator of chemotaxis, which upon deletion, increased indigoidine titers and was crucial to reweighting the metabolic model for the fourth and final DBTL cycle. Proteomics information sits in the "sweet spot" for characterizing cellular processes; it provides a rapid, semi-quantitative characterization of many activities much wider than metabolomics and can more directly implicate the cellular effectors than whole-genome resequencing. Our analysis pipelines are generalizable as preparing cells for proteomic analysis is an accessible method for hard to lyse microbes like corynebacteria or filamentous yeasts, where rapid metabolite quenching is challenging.[76,77]

In conclusion, the multiple iterations represent four DBTL cycles in this study that achieved high titer, rate, and yield (TRY) starting with GSMM predictions and the triple-gene-deletion strain. This mutant strain was subject to ALE to address oxidative stress, transcriptional regulation, and inefficient substrate catabolism. The final strain produced 7.3 g/L indigoidine at 77% MTY in M9 *p*-CA minimal salt medium. Aided by rapid strain engineering, we implemented learnings from comprehensive cellular analyses to maximize TRY. Achieving these metrics enable scaleup of valuable compounds like indigoidine, which enable biomanufacturing in many downstream applications.[38,39,78] This workflow is a blueprint for catalyzing other processes applied generally for multiple microbes, carbon streams, and final products.

Limitations of this study

Our multimodal analysis of *p*-CA/indigoidine growth-coupled strains identified coding sequence changes (via DNA resequencing) and differential protein expression (via proteomics), but not all known proteins predicted from the *P. putida* genome sequence are quantifiable. The MS-based method will not detect low-abundance proteins or proteins lacking trypsin digestion sites. Additionally, proteins embedded in membrane lipid bilayers are difficult to solubilize and are unlikely to be detected. Post-translational modifications can be difficult to detect by MS methods, and long noncoding RNAs or sRNAs cannot be accounted for their potential roles without developing new methods for RNA-seq in this bacterium. Finally, extending this method to other organisms lacking relevant information in the GSMMs limits model fidelity, which might be addressed with well-curated kinetic metabolic models or broadening the computational search space with alternative optimization algorithms such as OptKnock[79] or OptForce.[68]

STAR★METHODS

Detailed methods are provided in the online version of this paper and include the following:

- KEY RESOURCES TABLE
- RESOURCE AVAILABILITY
    - ○ Lead contact
    - ○ Materials availability
    - ○ Data and code availability
- EXPERIMENTAL MODEL AND STUDY PARTICIPANT DETAILS
- METHOD DETAILS
    - ○ Computation of constrained minimal cut sets
    - ○ Computation of elementary modes
    - ○ Validation of constrained minimal cut sets with constraint-based methods
    - ○ Proteomics data integration to create context specific models
    - ○ Nanopore + illumina hybrid method DNA assembly, SNP analysis
- QUANTIFICATION AND STATISTICAL ANALYSIS
    - ○ Molecular biology
    - ○ Construction of targeted genomic mutants in *P. putida* via allelic exchange or recombineering
    - ○ Preparation of stock *p*-CA
    - ○ Cultivation of *P. putida* for growth and production of indigoidine
    - ○ Glassware
    - ○ Kinetic growth curves
    - ○ Adaptive laboratory evolution
    - ○ Peroxide sensitivity assay
    - ○ Microbial interaction assay
    - ○ Soft X-Ray tomography characterization of cells
    - ○ Shotgun proteomics analysis
    - ○ TCA metabolite targeted analysis of growth coupled strains
    - ○ Analytical methods for the quantification of aromatics
    - ○ Purification of indigoidine used for product quantification and verification of purity by NMR
    - ○ Colorimetric determination of indigoidine from crude sample extracts
    - ○ LC-MS-based methods for the quantification of indigoidine
    - ○ Generation of BCD liquor of lignin from [Ch]Lys]-pretreated sorghum

SUPPLEMENTAL INFORMATION

Supplemental information can be found online at https://doi.org/10.1016/j.celrep.2023.113087.

ACKNOWLEDGMENTS

We thank Jeff Czajka (PNNL), Hyungyu Lim (Inha University), Adam Feist (UC San Diego), Corinne Scown (LBNL), and the Mukhopadhyay group for constructive feedback. T.E., D.B., J.M., Y.C., H.C., E.B., R.K., Y.L.D., J.G., C.J.P., B.S., J.D.K., and A.M. are funded by the U.S. Department of Energy (DOE) – BER JBEI project (DE-AC02-05CH11231 subcontract between Lawrence Berkeley National Laboratory and the U.S. Department of Energy). H.C. and J.G. are funded through Sandia National Laboratories, which is a multi-mission laboratory managed and operated by National Technology and Engineering Solutions of Sandia, LLC., a wholly owned subsidiary of Honeywell International, Inc., via the U.S. Department of Energy's National Nuclear Security Administration under contract DE-NA0003525. We thank Idaho National Labs (Idaho Falls, ID) for supplying the *Sorghum bicolor*. J.H.C., A.E., and C.L. are funded by the National Center for X-Ray Tomography and the Advanced Light Source, an Office of Science User Facility operated for the U.S. DOE, Office of Science by Lawrence Berkeley National Laboratory (DE-AC02-05CH11231). SXT data collection and analysis was partially supported by the National Institutes of Health grant P30 GM138441.

AUTHOR CONTRIBUTIONS

Molecular biology and strain engineering: T.E., J.M., D.B., and A.C. Computation of growth-coupled designs and metabolic flux analysis: D.B. Analytical chemistry: E.B., R.K., and Y.L.D. Proteomics: Y.C., J.G., and C.J.P. X-ray tomography: J.H.C., A.E., and C.L. Generation of BCD liquor: H.C. and J.G. Supervision, formal analysis, and acquisition of funds: A.M., J.D.K., B.A.S., and C.J.P. Drafted the manuscript: T.E., D.B., and A.M. All authors have read, provided feedback, and approved the manuscript for publication.

DECLARATION OF INTERESTS

J.D.K. has a financial interest in Amyris, Lygos, Demetrix, Napigen, Apertor Pharmaceuticals, Maple Bio, Ansa Biotechnologies, Berkeley Yeast, and Zero Acre Farms. T.E., D.B., and A.M. have submitted a patent related to the work described in this study (U.S. Patent Application No: 63/490,452).

INCLUSION AND DIVERSITY

One or more of the authors of this paper self-identifies as an underrepresented ethnic minority in their field of research or within their geographical location.

One or more of the authors of this paper self-identifies as a gender minority in their field of research. One or more of the authors of this paper self-identifies as a member of the LGBTQIA+ community. While citing references scientifically relevant for this work, we also actively worked to promote gender balance in our reference list.

Received: April 25, 2023
Revised: July 10, 2023
Accepted: August 18, 2023
Published: September 3, 2023

REFERENCES

1. Skinnider, M.A., Johnston, C.W., Gunabalasingam, M., Merwin, N.J., Kieliszek, A.M., MacLellan, R.J., Li, H., Ranieri, M.R.M., Webster, A.L.H., Cao, M.P.T., et al. (2020). Comprehensive prediction of secondary metabolite structure and biological activity from microbial genome sequences. Nat. Commun. *11*, 6058. https://doi.org/10.1038/s41467-020-19986-1.
2. Beller, H.R., Lee, T.S., and Katz, L. (2015). Natural products as biofuels and bio-based chemicals: fatty acids and isoprenoids. Nat. Prod. Rep. *32*, 1508–1526. https://doi.org/10.1039/c5np00068h.
3. Skoog, E., Shin, J.H., Saez-Jimenez, V., Mapelli, V., and Olsson, L. (2018). Biobased adipic acid - The challenge of developing the production host. Biotechnol. Adv. *36*, 2248–2263. https://doi.org/10.1016/j.biotechadv.2018.10.012.
4. Keasling, J., Garcia Martin, H., Lee, T.S., Mukhopadhyay, A., Singer, S.W., and Sundstrom, E. (2021). Microbial production of advanced biofuels. Nat. Rev. Microbiol. *19*, 701–715. https://doi.org/10.1038/s41579-021-00577-w.
5. Blöbaum, L., Haringa, C., and Grünberger, A. (2023). Microbial lifelines in bioprocesses: From concept to application. Biotechnol. Adv. *62*, 108071. https://doi.org/10.1016/j.biotechadv.2022.108071.
6. Wehrs, M., Tanjore, D., Eng, T., Lievense, J., Pray, T.R., and Mukhopadhyay, A. (2019). Engineering Robust Production Microbes for Large-Scale Cultivation. Trends Microbiol. *27*, 524–537. https://doi.org/10.1016/j.tim.2019.01.006.
7. Scown, C.D., Baral, N.R., Yang, M., Vora, N., and Huntington, T. (2021). Technoeconomic analysis for biofuels and bioproducts. Curr. Opin. Biotechnol. *67*, 58–64. https://doi.org/10.1016/j.copbio.2021.01.002.
8. Ögmundarson, Ó., Sukumara, S., Herrgård, M.J., and Fantke, P. (2020). Combining environmental and economic performance for bioprocess optimization. Trends Biotechnol. *38*, 1203–1214. https://doi.org/10.1016/j.tibtech.2020.04.011.
9. Liu, Z.-H., Hao, N., Wang, Y.-Y., Dou, C., Lin, F., Shen, R., Bura, R., Hodge, D.B., Dale, B.E., Ragauskas, A.J., et al. (2021). Transforming biorefinery designs with "Plug-In Processes of Lignin" to enable economic waste valorization. Nat. Commun. *12*, 3912. https://doi.org/10.1038/s41467-021-23920-4.
10. Corona, A., Biddy, M.J., Vardon, D.R., Birkved, M., Hauschild, M.Z., and Beckham, G.T. (2018). Life cycle assessment of adipic acid production from lignin. Green Chem. *20*, 3857–3866. https://doi.org/10.1039/C8GC00868J.
11. Bartling, A.W., Stone, M.L., Hanes, R.J., Bhatt, A., Zhang, Y., Biddy, M.J., Davis, R., Kruger, J.S., Thornburg, N.E., Luterbacher, J.S., et al. (2021). Techno-economic analysis and life cycle assessment of a biorefinery utilizing reductive catalytic fractionation. Energy Environ. Sci. *14*, 4147–4168. https://doi.org/10.1039/D1EE01642C.
12. del Río, J.C., Rencoret, J., Gutiérrez, A., Elder, T., Kim, H., and Ralph, J. (2020). Lignin Monomers from beyond the Canonical Monolignol Biosynthetic Pathway: Another Brick in the Wall. ACS Sustain. Chem. Eng. *8*, 4997–5012. https://doi.org/10.1021/acssuschemeng.0c01109.
13. Cao, L., Yu, I.K.M., Liu, Y., Ruan, X., Tsang, D.C.W., Hunt, A.J., Ok, Y.S., Song, H., and Zhang, S. (2018). Lignin valorization for the production of renewable chemicals: State-of-the-art review and future prospects. Bioresour. Technol. *269*, 465–475. https://doi.org/10.1016/j.biortech.2018.08.065.
14. Park, M.R., Chen, Y., Thompson, M., Benites, V.T., Fong, B., Petzold, C.J., Baidoo, E.E.K., Gladden, J.M., Adams, P.D., Keasling, J.D., et al. (2020). Response of *Pseudomonas putida* to Complex, Aromatic-Rich Fractions from Biomass. ChemSusChem *13*, 4455–4467. https://doi.org/10.1002/cssc.202000268.
15. Rodriguez, A., Salvachúa, D., Katahira, R., Black, B.A., Cleveland, N.S., Reed, M., Smith, H., Baidoo, E.E.K., Keasling, J.D., Simmons, B.A., Beckham, G.T., and Gladden, J.M. (2017). Base-Catalyzed Depolymerization of Solid Lignin-Rich Streams Enables Microbial Conversion. ACS Sustain Chem Eng *5*, 8171–8180. https://doi.org/10.1021/acssuschemeng.7b01818.
16. Mottiar, Y., Smith, R.A., Karlen, S.D., Ralph, J., and Mansfield, S.D. (2023). Evolution of p-coumaroylated lignin in eudicots provides new tools for cell wall engineering. New Phytol. *237*, 251–264. https://doi.org/10.1111/nph.18518.
17. Smith, R.A., Lu, F., Muro-Villanueva, F., Cusumano, J.C., Chapple, C., and Ralph, J. (2022). Manipulation of Lignin Monomer Composition Combined with the Introduction of Monolignol Conjugate Biosynthesis Leads to Synergistic Changes in Lignin Structure. Plant Cell Physiol. *63*, 744–754. https://doi.org/10.1093/pcp/pcac031.
18. Jiménez, J.I., Miñambres, B., García, J.L., and Díaz, E. (2002). Genomic analysis of the aromatic catabolic pathways from Pseudomonas putida KT2440. Environ. Microbiol. *4*, 824–841. https://doi.org/10.1046/j.1462-2920.2002.00370.x.
19. Thompson, M.G., Incha, M.R., Pearson, A.N., Schmidt, M., Sharpless, W.A., Eiben, C.B., Cruz-Morales, P., Blake-Hedges, J.M., Liu, Y., Adams, C.A., et al. (2020). Fatty acid and alcohol metabolism in Pseudomonas putida: functional analysis using random barcode transposon sequencing. Appl. Environ. Microbiol. *86*, e01665-20. https://doi.org/10.1128/AEM.01665-20.
20. Johnson, C.W., Salvachúa, D., Rorrer, N.A., Black, B.A., Vardon, D.R., St. John, P.C., Cleveland, N.S., Dominick, G., Elmore, J.R., Grundl, N., et al. (2019). Innovative Chemicals and Materials from Bacterial Aromatic Catabolic Pathways. Joule *3*, 1523–1537. https://doi.org/10.1016/j.joule.2019.05.011.
21. Almqvist, H., Veras, H., Li, K., Garcia Hidalgo, J., Hulteberg, C., Gorwa-Grauslund, M., Skorupa Parachin, N., and Carlquist, M. (2021). Muconic Acid Production Using Engineered *Pseudomonas putida* KT2440 and a Guaiacol-Rich Fraction Derived from Kraft Lignin. ACS Sustain. Chem. Eng. *9*, 8097–8106. https://doi.org/10.1021/acssuschemeng.1c00933.

22. Loeschcke, A., and Thies, S. (2015). Pseudomonas putida-a versatile host for the production of natural products. Appl. Microbiol. Biotechnol. *99*, 6197–6214. https://doi.org/10.1007/s00253-015-6745-4.

23. Zamboni, N., Fendt, S.-M., Rühl, M., and Sauer, U. (2009). (13)C-based metabolic flux analysis. Nat. Protoc. *4*, 878–892. https://doi.org/10.1038/nprot.2009.58.

24. Kukurugya, M.A., Mendonca, C.M., Solhtalab, M., Wilkes, R.A., Thannhauser, T.W., and Aristilde, L. (2019). Multi-omics analysis unravels a segregated metabolic flux network that tunes co-utilization of sugar and aromatic carbons in Pseudomonas putida. J. Biol. Chem. *294*, 8464–8479. https://doi.org/10.1074/jbc.RA119.007885.

25. Wilkes, R.A., Waldbauer, J., Caroll, A., Nieto-Domínguez, M., Parker, D.J., Zhang, L., Guss, A.M., and Aristilde, L. (2023). Complex regulation in a Comamonas platform for diverse aromatic carbon metabolism. Nat. Chem. Biol. *19*, 651–662. https://doi.org/10.1038/s41589-022-01237-7.

26. Meadows, A.L., Hawkins, K.M., Tsegaye, Y., Antipov, E., Kim, Y., Raetz, L., Dahl, R.H., Tai, A., Mahatdejkul-Meadows, T., Xu, L., et al. (2016). Rewriting yeast central carbon metabolism for industrial isoprenoid production. Nature *537*, 694–697. https://doi.org/10.1038/nature19769.

27. Lo, T.-M., Chng, S.H., Teo, W.S., Cho, H.-S., and Chang, M.W. (2016). A Two-Layer Gene Circuit for Decoupling Cell Growth from Metabolite Production. Cell Syst. *3*, 133–143. https://doi.org/10.1016/j.cels.2016.07.012.

28. Korman, T.P., Opgenorth, P.H., and Bowie, J.U. (2017). A synthetic biochemistry platform for cell free production of monoterpenes from glucose. Nat. Commun. *8*, 15526. https://doi.org/10.1038/ncomms15526.

29. Kim, J.-W., Lee, Y.-G., Kim, S.-J., Jin, Y.-S., and Seo, J.-H. (2019). Deletion of glycerol-3-phosphate dehydrogenase genes improved 2,3-butanediol production by reducing glycerol production in pyruvate decarboxylase-deficient Saccharomyces cerevisiae. J. Biotechnol. *304*, 31–37. https://doi.org/10.1016/j.jbiotec.2019.08.009.

30. Yim, H., Haselbeck, R., Niu, W., Pujol-Baxley, C., Burgard, A., Boldt, J., Khandurina, J., Trawick, J.D., Osterhout, R.E., Stephen, R., et al. (2011). Metabolic engineering of Escherichia coli for direct production of 1,4-butanediol. Nat. Chem. Biol. *7*, 445–452. https://doi.org/10.1038/nchembio.580.

31. Banerjee, D., Eng, T., Lau, A.K., Sasaki, Y., Wang, B., Chen, Y., Prahl, J.-P., Singan, V.R., Herbert, R.A., Liu, Y., et al. (2020). Genome-scale metabolic rewiring improves titers rates and yields of the non-native product indigoidine at scale. Nat. Commun. *11*, 5385. https://doi.org/10.1038/s41467-020-19171-4.

32. Harder, B.-J., Bettenbrock, K., and Klamt, S. (2016). Model-based metabolic engineering enables high yield itaconic acid production by Escherichia coli. Metab. Eng. *38*, 29–37. https://doi.org/10.1016/j.ymben.2016.05.008.

33. Mehrer, C.R., Rand, J.M., Incha, M.R., Cook, T.B., Demir, B., Motagamwala, A.H., Kim, D., Dumesic, J.A., and Pfleger, B.F. (2019). Growth-coupled bioconversion of levulinic acid to butanone. Metab. Eng. *55*, 92–101. https://doi.org/10.1016/j.ymben.2019.06.003.

34. Maia, P., Rocha, M., and Rocha, I. (2016). In Silico Constraint-Based Strain Optimization Methods: the Quest for Optimal Cell Factories. Microbiol. Mol. Biol. Rev. *80*, 45–67. https://doi.org/10.1128/MMBR.00014-15.

35. Zheng, Y., Liu, Q., Li, L., Qin, W., Yang, J., Zhang, H., Jiang, X., Cheng, T., Liu, W., Xu, X., and Xian, M. (2013). Metabolic engineering of Escherichia coli for high-specificity production of isoprenol and prenol as next generation of biofuels. Biotechnol. Biofuels *6*, 57. https://doi.org/10.1186/1754-6834-6-57.

36. García, B., Olivera, E.R., Miñambres, B., Fernández-Valverde, M., Cañedo, L.M., Prieto, M.A., García, J.L., Martínez, M., and Luengo, J.M. (1999). Novel biodegradable aromatic plastics from a bacterial source. Genetic and biochemical studies on a route of the phenylacetyl-coa catabolon. J. Biol. Chem. *274*, 29228–29241. https://doi.org/10.1074/jbc.274.41.29228.

37. von Kamp, A., and Klamt, S. (2017). Growth-coupled overproduction is feasible for almost all metabolites in five major production organisms. Nat. Commun. *8*, 15956. https://doi.org/10.1038/ncomms15956.

38. Takahashi, H., Kumagai, T., Kitani, K., Mori, M., Matoba, Y., and Sugiyama, M. (2007). Cloning and characterization of a *Streptomyces* single module type non-ribosomal peptide synthetase catalyzing a blue pigment synthesis. J. Biol. Chem. *282*, 9073–9081. https://doi.org/10.1074/jbc.M611319200.

39. Ghiffary, M.R., Prabowo, C.P.S., Sharma, K., Yan, Y., Lee, S.Y., and Kim, H.U. (2021). High-Level Production of the Natural Blue Pigment Indigoidine from Metabolically Engineered *Corynebacterium glutamicum* for Sustainable Fabric Dyes. ACS Sustain. Chem. Eng. *9*, 6613–6622. https://doi.org/10.1021/acssuschemeng.0c09341.

40. Wu, X., Galkin, M.V., Stern, T., Sun, Z., and Barta, K. (2022). Fully lignocellulose-based PET analogues for the circular economy. Nat. Commun. *13*, 3376. https://doi.org/10.1038/s41467-022-30735-4.

41. Wetmore, K.M., Price, M.N., Waters, R.J., Lamson, J.S., He, J., Hoover, C.A., Blow, M.J., Bristow, J., Butland, G., Arkin, A.P., and Deutschbauer, A. (2015). Rapid quantification of mutant fitness in diverse bacteria by sequencing randomly bar-coded transposons. mBio *6*, e00306–e00315. https://doi.org/10.1128/mBio.00306-15.

42. Sarsani, V., Aldikacti, B., He, S., Zeinert, R., Chien, P., and Flaherty, P. (2022). Model-based identification of conditionally-essential genes from transposon-insertion sequencing data. PLoS Comput. Biol. *18*, e1009273. https://doi.org/10.1371/journal.pcbi.1009273.

43. Fong, S.S., Burgard, A.P., Herring, C.D., Knight, E.M., Blattner, F.R., Maranas, C.D., and Palsson, B.O. (2005). In silico design and adaptive evolution of Escherichia coli for production of lactic acid. Biotechnol. Bioeng. *91*, 643–648. https://doi.org/10.1002/bit.20542.

44. Luo, H., and Hansen, A.S.L. (2018). Method of Improving Methyltransferase Activity. US Patent Application Number US16/469,039. International Patent Application Number WO2018037098A1.

45. Sandberg, T.E., Salazar, M.J., Weng, L.L., Palsson, B.O., and Feist, A.M. (2019). The emergence of adaptive laboratory evolution as an efficient tool for biological discovery and industrial biotechnology. Metab. Eng. *56*, 1–16. https://doi.org/10.1016/j.ymben.2019.08.004.

46. Trinh, C.T., and Srienc, F. (2009). Metabolic engineering of Escherichia coli for efficient conversion of glycerol to ethanol. Appl. Environ. Microbiol. *75*, 6696–6705. https://doi.org/10.1128/AEM.00670-09.

47. Alves, N.J., Turner, K.B., Daniele, M.A., Oh, E., Medintz, I.L., and Walper, S.A. (2015). Bacterial Nanobioreactors–Directing Enzyme Packaging into Bacterial Outer Membrane Vesicles. ACS Appl. Mater. Interfaces *7*, 24963–24972. https://doi.org/10.1021/acsami.5b08811.

48. Vermaas, J.V., Crowley, M.F., and Beckham, G.T. (2022). Molecular simulation of lignin-related aromatic compound permeation through gram-negative bacterial outer membranes. J. Biol. Chem. *298*, 102627. https://doi.org/10.1016/j.jbc.2022.102627.

49. Xu, Z., Peng, B., Kitata, R.B., Nicora, C.D., Weitz, K.K., Pu, Y., Shi, T., Cort, J.R., Ragauskas, A.J., and Yang, B. (2022). Understanding of bacterial lignin extracellular degradation mechanisms by Pseudomonas putida KT2440 via secretomic analysis. Biotechnol. Biofuels Bioprod. *15*, 117. https://doi.org/10.1186/s13068-022-02214-x.

50. Salvachúa, D., Werner, A.Z., Pardo, I., Michalska, M., Black, B.A., Donohoe, B.S., Haugen, S.J., Katahira, R., Notonier, S., Ramirez, K.J., et al. (2020). Outer membrane vesicles catabolize lignin-derived aromatic compounds in Pseudomonas putida KT2440. Proc. Natl. Acad. Sci. USA *117*, 9302–9310. https://doi.org/10.1073/pnas.1921073117.

51. Loconte, V., Chen, J.-H., Vanslembrouck, B., Ekman, A.A., McDermott, G., Le Gros, M.A., and Larabell, C.A. (2023). Soft X-ray tomograms provide a structural basis for whole-cell modeling. Faseb. J. *37*, e22681. https://doi.org/10.1096/fj.202200253R.

52. Odermatt, P.D., Miettinen, T.P., Lemière, J., Kang, J.H., Bostan, E., Manalis, S.R., Huang, K.C., and Chang, F. (2021). Variations of intracellular

density during the cell cycle arise from tip-growth regulation in fission yeast. Elife *10*, e64901. https://doi.org/10.7554/eLife.64901.

53. Eng, T., Herbert, R.A., Martinez, U., Wang, B., Chen, J.C., Brown, J.B., Deutschbauer, A.M., Bissell, M.J., Mortimer, J.C., and Mukhopadhyay, A. (2020). Iron Supplementation Eliminates Antagonistic Interactions Between Root-Associated Bacteria. Front. Microbiol. *11*, 1742. https://doi.org/10.3389/fmicb.2020.01742.
54. Luu, R.A., Kootstra, J.D., Nesteryuk, V., Brunton, C.N., Parales, J.V., Ditty, J.L., and Parales, R.E. (2015). Integration of chemotaxis, transport and catabolism in Pseudomonas putida and identification of the aromatic acid chemoreceptor PcaY. Mol. Microbiol. *96*, 134–147. https://doi.org/10.1111/mmi.12929.
55. Hekkelman, M.L., de Vries, I., Joosten, R.P., and Perrakis, A. (2023). AlphaFill: enriching AlphaFold models with ligands and cofactors. Nat. Methods *20*, 205–213. https://doi.org/10.1038/s41592-022-01685-y.
56. Nikel, P.I., Fuhrer, T., Chavarría, M., Sánchez-Pascuala, A., Sauer, U., and de Lorenzo, V. (2021). Reconfiguration of metabolic fluxes in Pseudomonas putida as a response to sub-lethal oxidative stress. ISME J. *15*, 1751–1766. https://doi.org/10.1038/s41396-020-00884-9.
57. Chubukov, V., Mingardon, F., Schackwitz, W., Baidoo, E.E.K., Alonso-Gutierrez, J., Hu, Q., Lee, T.S., Keasling, J.D., and Mukhopadhyay, A. (2015). Acute Limonene Toxicity in Escherichia coli Is Caused by Limonene Hydroperoxide and Alleviated by a Point Mutation in Alkyl Hydroperoxidase AhpC. Appl. Environ. Microbiol. *81*, 4690–4696. https://doi.org/10.1128/AEM.01102-15.
58. Forrester, S.J., Kikuchi, D.S., Hernandes, M.S., Xu, Q., and Griendling, K.K. (2018). Reactive oxygen species in metabolic and inflammatory signaling. Circ. Res. *122*, 877–902. https://doi.org/10.1161/CIRCRESAHA.117.311401.
59. Esterházy, D., King, M.S., Yakovlev, G., and Hirst, J. (2008). Production of reactive oxygen species by complex I (NADH:ubiquinone oxidoreductase) from Escherichia coli and comparison to the enzyme from mitochondria. Biochemistry *47*, 3964–3971. https://doi.org/10.1021/bi702243b.
60. Meehan, B.M., and Malamy, M.H. (2012). Fumarate reductase is a major contributor to the generation of reactive oxygen species in the anaerobe Bacteroides fragilis. Microbiology (Reading, Engl) *158*, 539–546. https://doi.org/10.1099/mic.0.054403-0.
61. Messner, K.R., and Imlay, J.A. (2002). Mechanism of superoxide and hydrogen peroxide formation by fumarate reductase, succinate dehydrogenase, and aspartate oxidase. J. Biol. Chem. *277*, 42563–42571. https://doi.org/10.1074/jbc.M204958200.
62. Korshunov, S., and Imlay, J.A. (2010). Two sources of endogenous hydrogen peroxide in Escherichia coli. Mol. Microbiol. *75*, 1389–1401. https://doi.org/10.1111/j.1365-2958.2010.07059.x.
63. Blanco-Romero, E., Redondo-Nieto, M., Martínez-Granero, F., Garrido-Sanz, D., Ramos-González, M.I., Martín, M., and Rivilla, R. (2018). Genome-wide analysis of the FleQ direct regulon in Pseudomonas fluorescens F113 and Pseudomonas putida KT2440. Sci. Rep. *8*, 13145. https://doi.org/10.1038/s41598-018-31371-z.
64. Martínez-García, E., Nikel, P.I., Chavarría, M., and de Lorenzo, V. (2014). The metabolic cost of flagellar motion in Pseudomonas putida KT2440. Environ. Microbiol. *16*, 291–303. https://doi.org/10.1111/1462-2920.12309.
65. Zur, H., Ruppin, E., and Shlomi, T. (2010). iMAT: an integrative metabolic analysis tool. Bioinformatics *26*, 3140–3142. https://doi.org/10.1093/bioinformatics/btq602.
66. Eng, T., Banerjee, D., Lau, A.K., Bowden, E., Herbert, R.A., Trinh, J., Prahl, J.-P., Deutschbauer, A., Tanjore, D., and Mukhopadhyay, A. (2021). Engineering Pseudomonas putida for efficient aromatic conversion to bioproduct using high throughput screening in a bioreactor. Metab. Eng. *66*, 229–238. https://doi.org/10.1016/j.ymben.2021.04.015.
67. Banerjee, D., and Mukhopadhyay, A. (2023). Perspectives in growth production trade-off in microbial bioproduction. RSC Sustain. *1*, 224–233. https://doi.org/10.1039/D2SU00066K.
68. Ranganathan, S., Suthers, P.F., and Maranas, C.D. (2010). OptForce: an optimization procedure for identifying all genetic manipulations leading to targeted overproductions. PLoS Comput. Biol. *6*, e1000744. https://doi.org/10.1371/journal.pcbi.1000744.
69. Tokic, M., Hatzimanikatis, V., and Miskovic, L. (2020). Large-scale kinetic metabolic models of Pseudomonas putida KT2440 for consistent design of metabolic engineering strategies. Biotechnol. Biofuels *13*, 33. https://doi.org/10.1186/s13068-020-1665-7.
70. Van Hofwegen, D.J., Hovde, C.J., and Minnich, S.A. (2016). Rapid Evolution of Citrate Utilization by Escherichia coli by Direct Selection Requires citT and dctA. J. Bacteriol. *198*, 1022–1034. https://doi.org/10.1128/JB.00831-15.
71. Lim, H.G., Eng, T., Banerjee, D., Alarcon, G., Lau, A.K., Park, M.-R., Simmons, B.A., Palsson, B.O., Singer, S.W., Mukhopadhyay, A., and Feist, A.M. (2021). Generation of *Pseudomonas putida* KT2440 Strains with Efficient Utilization of Xylose and Galactose via Adaptive Laboratory Evolution. ACS Sustain. Chem. Eng. *9*, 11512–11523. https://doi.org/10.1021/acssuschemeng.1c03765.
72. Gao, J., Li, Y., Yu, W., and Zhou, Y.J. (2022). Rescuing yeast from cell death enables overproduction of fatty acids from sole methanol. Nat. Metab. *4*, 932–943. https://doi.org/10.1038/s42255-022-00601-0.
73. Bajić, D., Vila, J.C.C., Blount, Z.D., and Sánchez, A. (2018). On the deformability of an empirical fitness landscape by microbial evolution. Proc. Natl. Acad. Sci. USA *115*, 11286–11291. https://doi.org/10.1073/pnas.1808485115.
74. Mohamed, E.T., Werner, A.Z., Salvachúa, D., Singer, C.A., Szostkiewicz, K., Rafael Jiménez-Díaz, M., Eng, T., Radi, M.S., Simmons, B.A., Mukhopadhyay, A., et al. (2020). Adaptive laboratory evolution of Pseudomonas putida KT2440 improves p-coumaric and ferulic acid catabolism and tolerance. Metab. Eng. Commun. *11*, e00143. https://doi.org/10.1016/j.mec.2020.e00143.
75. Liu, H., Zhou, P., Qi, M., Guo, L., Gao, C., Hu, G., Song, W., Wu, J., Chen, X., Chen, J., et al. (2022). Enhancing biofuels production by engineering the actin cytoskeleton in Saccharomyces cerevisiae. Nat. Commun. *13*, 1886. https://doi.org/10.1038/s41467-022-29560-6.
76. Wellerdiek, M., Winterhoff, D., Reule, W., Brandner, J., and Oldiges, M. (2009). Metabolic quenching of Corynebacterium glutamicum: efficiency of methods and impact of cold shock. Bioproc. Biosyst. Eng. *32*, 581–592. https://doi.org/10.1007/s00449-008-0280-y.
77. Khanijou, J.K., Kulyk, H., Bergès, C., Khoo, L.W., Ng, P., Yeo, H.C., Helmy, M., Bellvert, F., Chew, W., and Selvarajoo, K. (2022). Metabolomics and modelling approaches for systems metabolic engineering. Metab. Eng. Commun. *15*, e00209. https://doi.org/10.1016/j.mec.2022.e00209.
78. Yumusak, C., Prochazkova, A.J., Apaydin, D.H., Seelajaroen, H., Sariciftci, N.S., Weiter, M., Krajcovic, J., Qin, Y., Zhang, W., Zhan, J., and Kovalenko, A. (2019). Indigoidine – Biosynthesized organic semiconductor. Dyes Pigments *171*, 107768. https://doi.org/10.1016/j.dyepig.2019.107768.
79. Burgard, A.P., Pharkya, P., and Maranas, C.D. (2003). Optknock: a bilevel programming framework for identifying gene knockout strategies for microbial strain optimization. Biotechnol. Bioeng. *84*, 647–657. https://doi.org/10.1002/bit.10803.
80. Wannier, T.M., Nyerges, A., Kuchwara, H.M., Czikkely, M., Balogh, D., Filsinger, G.T., Borders, N.C., Gregg, C.J., Lajoie, M.J., Rios, X., Pál, C., and Church, G.M. (2020). Improved bacterial recombineering by parallelized protein discovery. PNAS *117*, 13689–13698. https://doi.org/10.1073/pnas.200158811.
81. Nogales, J., Mueller, J., Gudmundsson, S., Canalejo, F.J., Duque, E., Monk, J., Feist, A.M., Ramos, J.L., Niu, W., and Palsson, B.O. (2020). High-quality genome-scale metabolic modelling of *Pseudomonas putida*

highlights its broad metabolic capabilities. Environ. Microbiol. *22*, 255–269. https://doi.org/10.1111/1462-2920.14843.

82. Klamt, S., Saez-Rodriguez, J., and Gilles, E.D. (2007). Structural and functional analysis of cellular networks with CellNetAnalyzer. BMC Syst. Biol. *1*, 2. https://doi.org/10.1186/1752-0509-1-2.
83. Terzer, M., and Stelling, J. (2008). Large-scale computation of elementary flux modes with bit pattern trees. Bioinformatics *24*, 2229–2235. https://doi.org/10.1093/bioinformatics/btn401.
84. Mahadevan, R., and Schilling, C.H. (2003). The effects of alternate optimal solutions in constraint-based genome-scale metabolic models. Metab. Eng. *5*, 264–276. https://doi.org/10.1016/j.ymben.2003.09.002.
85. Heirendt, L., Arreckx, S., Pfau, T., Mendoza, S.N., Richelle, A., Heinken, A., Haraldsdóttir, H.S., Wachowiak, J., Keating, S.M., Vlasov, V., et al. (2019). Creation and analysis of biochemical constraint-based models using the COBRA Toolbox v.3.0. Nat. Protoc. *14*, 639–702. https://doi.org/10.1038/s41596-018-0098-2.
86. Langley, S., Eng, T., Wan, K.H., Herbert, R.A., Klein, A.P., Yoshikuni, Y., Tringe, S.G., Brown, J.B., Celniker, S.E., Mortimer, J.C., and Mukhopadhyay, A. (2019). Complete Genome Sequence of Agrobacterium sp. Strain 33MFTa1.1, Isolated from Thlaspi arvense Roots. Microbiol. Resour. Announc. *8*, e00432-19. https://doi.org/10.1128/MRA.00432-19.
87. Wick, R.R., Judd, L.M., Gorrie, C.L., and Holt, K.E. (2017). Unicycler: Resolving bacterial genome assemblies from short and long sequencing reads. PLoS Comput. Biol. *13*, e1005595. https://doi.org/10.1371/journal.pcbi.1005595.
88. Tatusova, T., DiCuccio, M., Badretdin, A., Chetvernin, V., Nawrocki, E.P., Zaslavsky, L., Lomsadze, A., Pruitt, K.D., Borodovsky, M., and Ostell, J. (2016). NCBI prokaryotic genome annotation pipeline. Nucleic Acids Res. *44*, 6614–6624. https://doi.org/10.1093/nar/gkw569.
89. Sambrook, J., and Russell, D.W. (2001). Molecular Cloning: A Laboratory Manual. In 3 Volume Set, Third Edition (Cold Spring Harbor Laboratory Press). 3rd ed.
90. Mamedov, T.G., Pienaar, E., Whitney, S.E., TerMaat, J.R., Carvill, G., Goliath, R., Subramanian, A., and Viljoen, H.J. (2008). A fundamental study of the PCR amplification of GC-rich DNA templates. Comput. Biol. Chem. *32*, 452–457. https://doi.org/10.1016/j.compbiolchem.2008.07.021.
91. Czajka, J.J., Banerjee, D., Eng, T., Menasalvas, J., Yan, C., Munoz, N.M., Poirier, B.C., Kim, Y.-M., Baker, S.E., Tang, Y.J., and Mukhopadhyay, A. (2022). Tuning a high performing multiplexed-CRISPRi Pseudomonas putida strain to further enhance indigoidine production. Metab. Eng. Commun. *15*, e00206. https://doi.org/10.1016/j.mec.2022.e00206.
92. Linger, J.G., Vardon, D.R., Guarnieri, M.T., Karp, E.M., Hunsinger, G.B., Franden, M.A., Johnson, C.W., Chupka, G., Strathmann, T.J., Pienkos, P.T., and Beckham, G.T. (2014). Lignin valorization through integrated biological funneling and chemical catalysis. Proc. Natl. Acad. Sci. USA *111*, 12013–12018. https://doi.org/10.1073/pnas.1410657111.
93. Jensen, H.M., Eng, T., Chubukov, V., Herbert, R.A., and Mukhopadhyay, A. (2017). Improving membrane protein expression and function using genomic edits. Sci. Rep. *7*, 13030. https://doi.org/10.1038/s41598-017-12901-7.
94. Chen, J.-H., Vanslembrouck, B., Loconte, V., Ekman, A., Cortese, M., Bartenschlager, R., McDermott, G., Larabell, C.A., Le Gros, M.A., and Weinhardt, V. (2022). A protocol for full-rotation soft X-ray tomography of single cells. STAR Protoc. *3*, 101176. https://doi.org/10.1016/j.xpro.2022.101176.
95. Parkinson, D.Y., Knoechel, C., Yang, C., Larabell, C.A., and Le Gros, M.A. (2012). Automatic alignment and reconstruction of images for soft X-ray tomography. J. Struct. Biol. *177*, 259–266. https://doi.org/10.1016/j.jsb.2011.11.027.
96. Ekman, A., Chen, J.-H., Dermott, G.M., Le Gros, M.A., and Larabell, C. (2020). Task Based Semantic Segmentation of Soft X-ray CT Images Using 3D Convolutional Neural Networks. Microsc. Microanal. *26*, 3152–3154. https://doi.org/10.1017/S1431927620023983.
97. Chen, Y., Gin, J., and Petzold, C.J. (2023). Alkaline-SDS Cell Lysis of Microbes with Acetone Protein Precipitation for Proteomic Sample Preparation in Protocols.Io. PLoS One *18*, e0288102. https://doi.org/10.17504/protocols.io.6qpvr6xjpvmk/v1.
98. Chen, Y., Gin, J., and Petzold, C.J. (2022). Discovery proteomic (DIA) LC-MS/MS data acquisition and analysis v2. Protocols.io. https://doi.org/10.17504/protocols.io.e6nvwk1z7vmk/v2.
99. Demichev, V., Messner, C.B., Vernardis, S.I., Lilley, K.S., and Ralser, M. (2020). DIA-NN: neural networks and interference correction enable deep proteome coverage in high throughput. Nat. Methods *17*, 41–44. https://doi.org/10.1038/s41592-019-0638-x.
100. Chen, Y., and Petzold, C.J. (2022). Label-free quantification (LFQ) proteomic data analysis from DIA-NN output files v2. Protocols.io. https://doi.org/10.17504/protocols.io.5qpvobk7xl4o/v2.
101. Amer, B., Kakumanu, R., and Baidoo, E.E. (2022). HILIC-MS analysis of central carbon metabolites in gram negative bacteria v1. Protocols.io. https://doi.org/10.17504/protocols.io.4r3l2opzxv1y/v1.
102. Rodriguez, A., Ersig, N., Geiselman, G.M., Seibel, K., Simmons, B.A., Magnuson, J.K., Eudes, A., and Gladden, J.M. (2019). Conversion of depolymerized sugars and aromatics from engineered feedstocks by two oleaginous red yeasts. Bioresour. Technol. *286*, 121365. https://doi.org/10.1016/j.biortech.2019.121365.
103. Eudes, A., Juminaga, D., Baidoo, E.E.K., Collins, F.W., Keasling, J.D., and Loqué, D. (2013). Production of hydroxycinnamoyl anthranilates from glucose in Escherichia coli. Microb. Cell Factories *12*, 62. https://doi.org/10.1186/1475-2859-12-62.
104. Wehrs, M., Gladden, J.M., Liu, Y., Platz, L., Prahl, J.-P., Moon, J., Papa, G., Sundstrom, E., Geiselman, G.M., Tanjore, D., et al. (2019). Sustainable bioproduction of the blue pigment indigoidine: Expanding the range of heterologous products in *R. toruloides* to include non-ribosomal peptides. Green Chem. *21*, 3394–3406. https://doi.org/10.1039/C9GC00920E.
105. Choudhary, H., Das, L., Pelton, J.G., Sheps, L., Simmons, B.A., Gladden, J.M., and Singh, S. (2023). Funneled Depolymerization of Ionic Liquid-Based Biorefinery "Heterogeneous" Lignin into Guaiacols over Reusable Palladium Catalyst. Chem. Eur J. *29*, e202300330. https://doi.org/10.1002/chem.202300330.

STAR★METHODS

KEY RESOURCES TABLE

REAGENT or RESOURCE	SOURCE	IDENTIFIER
Bacterial and virus strains		
NEB 10-beta Competent *E. coli* (High Efficiency)	New England Biolabs	C3019H
XL1-Blue Competent Cells	Agilent	200236
Pseudomonas putida KT2440	ATCC	47054
Biological samples		
Sorghum bicolor	Idaho National Laboratory (from Oklahoma State University)	Cultivar: Hybrid E5200 Sample: Split-2 Project: FY15 Reference Materials QR Code: 71109599-016D-4847-A87E-31E002C129C2
Chemicals, peptides, and recombinant proteins		
p-coumaric acid (*p*-coumarate)	Sigma Aldritch	C9008
Cholinium Lysinate	Proionic GmbH	01334.4000
Deposited data		
P. putida mutant genome resequencing (hybrid assembly)	NCBI Bioproject, Raw Reads	BioSample: SAMN33347499 - SAMN33347506
P. putida mutant genome resequencing (hybrid assembly)	NCBI, Assembled genomes	BioSample: SAMN33347507 - SAMN33347510
P. putida mutant genome resequencing (hybrid assembly)	NCBI, Annotated genomes with features	Biosample: CP118872 - CP118875
P. putida proteomics analysis	ProteomeXchange Consortium	ProteomeXchange: PXD040697
P. putida Soft X-Ray Tomography Raw Data	NCXT File Exchange	https://ncxt-nas1.lbl.gov:5001/sharing/TMeDj8LoZ
Experimental models: Organisms/strains		
Pseudomonas putida KT2440 - a complete list of modified strains can be found in Data S2	This paper	N/A
Oligonucleotides		
See Data S2 for all oligonucleotides used in this study.	This study	N/A
Recombinant DNA		
Refer to Data S2 for the gRNA sequences used in targeting Cpf1 for CRISPR mediated counterselection with recombineering.	This study	N/A
pORTMAGE-Pa1 {pmp-Pa.RecT,Pa.mutL-E36K xylS BBR1 aacC1}	Addgene No. 138,475	Wannier et al. 2020[80]
pTE302 {arap-Sc.bpsA,Bc.sfp-PP_5402-adjacent homology arms for integration KanMx6 sacB}	Banerjee et al., 2020[31]	N/A
Software and algorithms		
Prism 9.5.1	GraphPad Software	N/A
Geneious Prime	Dotmatics Inc	N/A
MATLAB R2017b	Mathworks	N/A
COBRA Toolbox	https://opencobra.github.io/cobratoolbox/stable/index.html	N/A

(*Continued on next page*)

Continued

REAGENT or RESOURCE	SOURCE	IDENTIFIER
Cell Net Analyzer	http://www2.mpi-magdeburg.mpg.de/projects/cna/cna.html	N/A
CPLEX Optimization Studio Version 12.8.0	IBM	N/A

RESOURCE AVAILABILITY

Lead contact

Further information and requests for resources and reagents should be directed to and will be fulfilled by the lead contact, Aindrila Mukhopadhyay (amukhopadhyay@lbl.gov)

Materials availability

Plasmids, plasmid sequences, and *P. putida* strains used in this manuscript have been deposited at the Joint BioEnergy Research Center Bioarchive at LBNL and can be requested at public-registry.jbei.org following execution of a completed Material Transfer Agreement.

Data and code availability

- All standardized proteomics and whole genome sequencing data is publicly available from datatype specific repositories. Sequencing data for strains described in this study have been deposited at NCBI under BioProject ID No. PRJNA937293. The raw reads for strains sequenced with Illumina short read and Oxford nanopore technology are deposited under BioSample No. SAMN33347499 - SAMN33347506. The assembled genomes have been deposited in the NCBI genome repository with BioSample No. SAMN33347507 - SAMN33347510 and their respective genome accession numbers CP118872 - CP118875. The generated mass spectrometry proteomics data have been deposited to the ProteomeXchange Consortium via the PRIDE (Perez-Riverol et al., 2022) partner repository with the dataset identifier PXD040697.
- All original code generated in this study is included in the supplementary data. Data S1 contains the small metabolic model used for elementary mode analysis calculations and the custom scripts used to analyze the modified PSP workflow in this study.
- Any additional information required to reanalyze the data reported in this work paper is available from the lead contact upon request.

EXPERIMENTAL MODEL AND STUDY PARTICIPANT DETAILS

Pseudomonas putida KT2440 (and its derivative strains) were routinely cultured using standard laboratory conditions in LB (Luria Bertani) medium (10 g/L tryptone, 5 g/L yeast extract, 10 g/L NaCl) provided by Millipore Sigma. When cells were cultured on petri dishes, LB media was supplemented with 2% (w/v) agar (Bectin Dickinson, Bacto Agar) and incubated at 30°C. Cryostocks were prepared by diluting bacterial cultures grown to saturation overnight to 25% (w/v) glycerol before storage at −80°C.

METHOD DETAILS

Computation of constrained minimal cut sets

Pseudomonas putida KT2440 genome scale metabolic model (GSMM) iJN1411 and iJN1463[81] were used. Aerobic conditions with *para*-coumarate (*p*-CA) as the sole carbon source were used to model growth parameters. In the GSMM, *p*-CA is represented as *Trans*-4-Hydroxycinnamate (t4hcinnm). The lower flux bounds for ATP maintenance demand and *para*-coumarate (*p*-CA) uptake were 0.97 mmol ATP/gDCW/h and −10 mmol *p*-CA/gDCW/h, respectively. Constrained minimal cut sets (cMCS) were calculated using the MCS algorithm[37] available as part of CellNetAnalyzer.[82] Excretion of byproducts was initially set to zero, except for the reported secreted products specific to *P. putida* (gluconate, 2-ketogluconate, 3-oxoadipate, catechol, lactate, ethanol, methanol, CO_2, and acetate) that had an upper flux bound of 1000 mmol/gDCW/h. We calculated the maximum theoretical yields (MTY) for indigoidine using *p*-CA as the carbon source and the heterologous 2 gene indigoidine production pathway. Additional inputs including minimum demanded product yield, YPS (10%–85% of MTY) and maximum demanded biomass yield, YBS, at 10 to 25% of maximum biomass yield were also specified in order to constrain the desired design space. The maximum size of cMCS was kept at the default (i.e., 50 metabolic reactions). Knockouts of export reactions and spontaneous reactions were not allowed. With the specifications used herein, each calculated knockout strategy (cMCS) demands production of indigoidine even when cells do not grow. Each cMCS computation run provides a prediction of several cMCS designs of the same cMCS size, but the cMCS sizes may vary depending on the additional inputs (YPS and YBS) for each run. All cMCS calculations were done using API functions of CellNetAnalyzer[82] on

MATLAB 2017b platform using CPLEX 12.8 as the MILP solver. The different runs, respective number of cut sets and number of targeted reactions to satisfy coupling constraints to scan a wide area of the search space are included in Table S2.

Computation of elementary modes

For elementary modes analysis, a small model representing the central carbon metabolism of *P. putida* and the heterologous indigoidine production pathway (Supplementary Data 3) was used to calculate elementary modes by *efmtool*.[83]

Validation of constrained minimal cut sets with constraint-based methods

The *P. putida* GSMM was extended to account for the indigoidine biosynthesis pathway and checked for strong growth coupling to confirm the chosen engineering strategy for experimental implementation as we have done previously.[31] The cytosolic reaction for indigoidine biosynthesis from glutamine was added as previously described.[31] Flux balance analysis (FBA) was used to calculate the maximum theoretical yield (MTY) from reaction stoichiometry and redox balance. Flux variability analysis (FVA) was used along with FBA to check for minimum and maximum glutamine or indigoidine flux under the identified cMCS strategy to confirm growth coupling. Standard FVA[84] was performed with biomass formation as the objective function and deletions of the proposed gene targets in each cMCS strategy along with constraints that were used for cMCS calculations. The lower bound for the indigoidine production was set to zero and the upper bound was left at maximum (i.e., 1000). Thus, we did not artificially enforce flux through this pathway. Instead, we verified the cMCS underlying assumptions were satisfied that resulted in strong coupled indigoidine production, i.e., maximum indigoidine production at all times. For Design One, after deleting the four genes (PP_1378, PP_0944, PP_1755 and PP_0897), using FBA we obtained a maximum biomass of 0.036/h with a *p*-CA uptake of 4.67 mmol/gDCW/h. FVA of Design One model predicted identical minimum and maximum indigoidine flux of 2.33 mmol/gDCW/h. A positive minimum and maximum flux through the exchange reaction for the metabolite of interest (glutamine or indigoidine) confirmed strong growth coupling. COBRA Toolbox v.3.0[85] in MATLAB R2017b was used for FBA and FVA simulations with the GLPK (https://gnu.org/software/glpk) or Gurobi Optimizer 8.1 (http://www.gurobi.com/) as the linear optimization solver.

Proteomics data integration to create context specific models

The proteomics data and the *P. putida* GSMM, iJN1463, were used to extract context specific models for the two Design 1 isolates. We used the integrated metabolic analysis tool (iMAT) algorithm,[65] which uses discrete levels for expression values: low, medium and high. iMAT allowed the integration of proteomics data into the GSMM and maximized highly and minimized lowly expressed reactions from the model. We used the $\log_2$ fold changes in protein counts with respect to WT in the two D1 isolates to perform this classification with a cutoff of half a standard deviation above the mean of the $\log_2$FC values, for active reactions, and half a standard deviation below for inactive reactions. The iMAT algorithm iteratively searches for a set of active reactions, within the cutoff range, linked to the levels of the associated proteins that simultaneously are able to result in biomass and indigoidine production. Simulations were performed using the iMAT implementation in the Cobra Toolbox with MATLAB 2017b (Mathworks Inc., Natick, MA, USA) and CPLEX 12.8 (IBM) as the solver.

Nanopore + illumina hybrid method DNA assembly, SNP analysis

P. putida genomic DNA of the indicated genotypes was prepared for whole genome sequencing and hybrid assembly using conventional laboratory techniques as previously described.[86] Briefly, cryostocks were struck to single colonies on LB agar medium and inoculated into liquid 5 mL LB cultures and incubated overnight at 30°C until saturated. Approximately 1.5 mL of cells were harvested, spun down (5,000 x *g*, 3 min), flash frozen and lysed (50 U/mL units RNAse, 0.1% w/v SDS, 200mM NaCl, pH 8) for genomic DNA extraction using 1.5 mL of cell culture with a phenol chloroform extraction and phase lock tubes (Qiagen Sciences, Germantown, MD) to enhance phase separation. Following isopropanol + NaOAc precipitation, the DNA pellet was washed twice with 70% ethanol and air dried before resuspension. Approximately 2 μg of DNA was used for either Illumina or Nanopore sequencing, conducted by SeqCenter Inc. (Pittsburgh, PA). For Illumina short read sequencing, sample libraries were prepared using the Illumina DNA Prep kit and IDT 10bp UDI indices and sequenced on an Illumina NextSeq 2000, producing 2x151bp reads. Demultiplexing, quality control and adapter trimming was performed with bcl-convert (v3.9.3) (Illumina Inc). Oxford Nanopore reads were processed for quality control and adapter trimming using porechop (github.com/rrwick/Porechop). Hybrid assembly with Illumina and ONT reads was performed with Unicycler.[87] Assembly statistics were recorded with QUAST. Annotations of protein-encoding open reading frames and noncoding RNAs (ncRNAs) were predicted with the NCBI Prokaryotic Genome Annotation Pipeline.[88] To map existing GeneID accession numbers (PP_XXXX) to the new chromosomal assemblies, we used the Geneious WGS software package (v10.0.1, BioMatters LTD). The new chromosomal assembly was aligned with the NCBI reference sequence (NC_002947.4) using Mauve and the transferred gene annotations were extracted as LCB (locally colinear blocks) alignment files. Single nucleotide polymorphisms and other variants were identified using the Geneious "Variations/SNP" (default settings for variant probability; bacterial translation start codon settings) tool comparing the mutant strains to either the WT strain or the pre-ALE Δ3 strain as indicated. 116 pre-existing mutations in the KT2440 genome and an additional 162 pre-existing mutations from the pre-ALE Δ3 genome assembly were removed from further analysis. Genome coverage via Illumina sequencing was at least 98-fold and at least 60-fold genome coverage with reads $\geq$2,000 bp in length for Nanopore sequencing. Each genome assembly produced a single ~6m bp circular chromosome as expected for *P. putida* KT2440. Chromosome topology was conserved from the reference NCBI genome to the resequenced WT hybrid assembly except for a 9kb inversion from PP_0001-PP_0009.

To identify unique polymorphisms in the Design 1 strains, we demanded that the mutation be absent in either the resequenced WT strain as well as the pre-ALE Δ3 strain. New mutants were binned into functional categories (Data S2) and their fitness defects on known substrates were examined on the fitness browser (fit.genomics.lbl.gov). Genes of unknown function were subject to hierarchical clustering to compare correlations with mutations in characterized genes for aromatic carbon sources.

QUANTIFICATION AND STATISTICAL ANALYSIS

The statistical analysis described in Figure 2C related to the quantification of cell size and density and exact number of cells (n) is described in the STAR Methods section "soft X-ray tomography characterization of cells." The standard deviation of OD values as a proxy for growth under the tested conditions is plotted as a shaded area between two solid lines, where the centered line represents the average value. The exact number of replicates averaged is described in the corresponding figure legend. For quantification of metabolites, details regarding the analysis and exact value of n are described in the STAR Methods section titled "TCA Metabolite Targeted Metabolomics analysis of growth coupled strains." Finally, the error bars regarding indigoidine titer and yield reflect the standard deviation between biological replicates with all individual data points shown in the figure panel.

Molecular biology

All strains, plasmids, and gRNA sequences used in this study are described in Data S2. Cloning of synthetic DNA constructs was conducted using chemically competent DH10-β cells purchased from NEB (New England Biolabs (NEB), Ipswitch, MA) or XL-1 Blue (Agilent Technologies, Santa Clara, CA)cells prepared for chemical competency using the Inuoe method[89] by the UC Berkeley QB3 Core facility (Berkeley, CA). Two constructs used for the initial multiplex CRISPRi/dCpf1 prototyping were synthesized by Genscript USA Inc (Piscataway, NJ) using the same logic for unique promoter-gRNA-terminator designs as described previously.[31] All DNA assemblies were designed using Snapgene (BioMatters Ltd). NEB OneTaq 2x PCR Master Mix was used for routine genotyping of *P. putida* transformants after recombineering or allelic exchange, and NEB Q5 2x PCR master mix was used to amplify DNA fragments for isothermal HiFi assembly (NEB). PCR and isothermal assembly were conducted following manufacturer's guidelines for extension time and annealing temperature. The annealing time was always set to 3 s.[90] Plasmids were transformed into *P. putida* strains of the indicated genotype via electroporation after 2 washes in 10% glycerol exactly as previously described.[31] Both *E. coli* and *P. putida* glycerol stocks were stored at −80°C using a final glycerol concentration of 25% (w/v). New gRNA designs were verified by Sanger sequencing (Azenta Life Sciences, Burlington, MA). Complex new DNA assemblies for heterologous gene pathways were verified by whole plasmid sequencing (Primordium Labs, Monrovia, CA). Kanamycin (50 μg/mL) or gentamicin (30 μg/mL) was added to the appropriate medium as indicated for experiments requiring the selection of plasmids. To assess strain viability using semi-quantitative serial dilution assays, strains were diluted 10x in a microtiter dish and 3 μL of diluted cells were plated on solid agar plates supplemented with LB and M9 media with additives as indicated and incubated at 30°C. LB plates were photographed after 24 h. M9 *p*-CA plates were photographed after 48 h. To determine the number of colony forming units present in 1 OD_{600} of culture media, overnight cultures grown at 30°C in 5mL culture tubes were diluted 50,000x in sterile media and vortexed thoroughly. 10 μL or 50 μL of the diluted culture was spread onto solid LB agar media and spread with a sterile rod or glass beads. Plates were incubated at 30°C overnight and CFUs were counted after incubation for 24 h.

Construction of targeted genomic mutants in *P. putida* via allelic exchange or recombineering

Generation of in-frame precise deletions in *P. putida* was implemented primarily using a recombineering/CRISPR counterselection protocol.[91] In brief, 90 bp ssDNA oligos were designed to bind 45 bp upstream and downstream precisely targeting the start and stop codons of the desired gene for removal. If the reading frame overlapped with other coding sequences, the deleted region was modified to exclude any bases that were necessary for expressing the overlapping coding sequences. All oligos were synthesized by IDT (Integrated DNA Technologies, Redwood City, CA) and are described in Data S2. Recombineering clones were selected using Cpf1-based counterselection with a 20–21 bp gRNA with homology for the WT locus of the targeted gene for deletion. gRNAs were designed by identifying a 5′-TTTN-3′ PAM sequence 5′ upstream of the locus targeted for recombineering. All gRNA sequences are described in Data S2. Cpf1/Cas12a endonuclease eliminates unedited cells by targeting the specified WT locus to generate a lethal double-strand break. After genotyping colonies by colony PCR and loss of the Cpf1-gRNA plasmid the process was repeated as needed. The inducer, 3-methyl-benzoate (3MB, *m*-toluic acid, Sigma T36609), was used at a concentration of 1mM. The 500 mM 3MB stock solution was dissolved in 50% ethanol/water, stored at 4°C, and discarded after 6 months. Gene deletions were confirmed by colony PCR genotyping using NEB Onetaq Quick-Load 2X Master Mix with Standard Buffer (Cat. No. M0486L) as described above following an initial colony boiling step (50 μL 20mM NaOH, 30 min, 98°C).

Several allelic exchange plasmids were also used for the integration of the original or variant heterologous indigoidine pathway, and for the deletion of PP_4120. Standard protocols for the initial integration, counterselection, and verification of strains by genotyping were executed without modification as previously described.[66]

Preparation of stock *p*-CA

A solution of *para*-coumarate (*p*-CA, 98% purity, Sigma Aldrich, Cat. No. C9008) was prepared at a concentration of 0.5 M by dissolving 20.52 g into 250 mL of sterile ddH_20 and pH adjusted to 8 using NaOH pellets (Cat. No. S8045) with stirring to ensure complete dissolution. Afterward, the solution was filter sterilized (0.2 μm SFC, Nalgene, Cat. No. 291–4520) and was discarded roughly after 3 months of storage at room temperature when the color changed from slightly amber to a dark brown. The rate of dark color appearance was not dependent on storage temperature, time of year, or exposure to ambient light, but may correlate with the age of specific batches purchased from the supplier.

Cultivation of *P. putida* for growth and production of indigoidine

An overnight LB liquid culture was prepared from a single colony struck out from cryostorage. M9 minimal medium used here was modified from the "NREL" formulation[92] to 100 mM NH_4Cl, 47.9 mM Na_2HPO_4, 22 mM KH_2PO_4, 8.56 mM NaCl, 2 mM $MgSO_4$, 100 μM $CaCl_2$ with 1X trace metals solution (Catalog Num. T1001, Teknova Inc, Hollister CA), 60 mM of *p*-CA and 30 mM of 3-(N-Morpholino)propanesulfonic acid (MOPS; (Sigma Catalog Num. M1254)) and set to a pH of 7.0 was used to test the performance of the strains, or with *p*-CA concentrations as otherwise indicated for C/N ratio analysis. To inoculate cells for adaptation, 500 μL (starting $OD_{600} = 0.4$) from a saturated LB overnight culture were added to a 5 mL of M9 *p*-CA medium in a culture tube. Cultures were incubated at 30°C with 200 rpm with orbital shaking and 40% humidity. A second adaptation was performed in M9 medium in the desired format for the production run. Unless otherwise indicated, the concentration of *p*-CA used for indigoidine production was 60 mM. When dCpf1/CRISPR plasmids were used for gene interference (CRISPRi) with Design I and Design II plasmids, 500 μM IPTG and 50 μg/mL kanamycin was added to the medium to induce the gRNA array and to maintain plasmid selection, respectively. IPTG was added at the same time the pathway was induced with arabinose. The majority of experiments here using the Design 1 strains did not require IPTG addition or plasmid selection during the indigoidine production runs with the exception of the proteomics data described in Figure 3B which used kanamycin for plasmid selection of the kanR + pTE449 empty vector transformed into all 3 strains. When cultivated in a 24-deep well plate (Axygen Scientific, Union City, CA) a 1.5 mL volume fill was used and the experiment was done in quadruplicates with linear shaking at 1,000 rpm, 30°C and 70% humidity using a gas-permeable film (114 μm AeraSeal Film, Omega Biotek, Cat. No. AC1201-02). For shake flask experiments, 20 mL or 50 mL cultures were grown in 250 mL Erlenmeyer baffled shake flasks with orbital shaking at 200 rpm in triplicates. Indigoidine pathway gene expression was induced with 0.3% w/v or 1.5% w/v arabinose as indicated in the figure legend. Error bars indicate the standard deviation between measurements.

Glassware

P. putida is growth-sensitive to residual detergents on glassware. Glassware was inspected before use for residual powder or debris before use. As needed, glassware was recleaned by triple rinsing with MilliQ grade ddH2O and 95% ethanol, which was repeated six times. Glassware was then resterilized by autoclaving.

Kinetic growth curves

A kinetic time course to monitor changes in optical density was used to measure at OD_{595} nm every 15 min using a Molecular Devices Filtermax F5 plate reader (Molecular Devices LLC, San Jose, CA) set to "high" shake speed and linear shaking mode in a 24 well microtiter dish plate sealed with a Breathe-Easy® transparent membrane (Sigma-Aldrich). For the data in Figure S5, a Molecular Devices Spectramax 5e was used to collect the timecourse by monitoring OD_{600} with the same plate format but sampled every 10 min for the duration of the timecourse. Microtiter plates were incubated at 30°C for the duration of the timecourse.

Adaptive laboratory evolution

We implemented adaptive laboratory evolution (ALE) using several different concurrent strategies and independent strain isolates. The goal of this ALE experiment was to restore growth of the engineered strains in M9 *p*-CA with *p*-CA concentrations exceeding 100 mM without a pre-determined maximum *p*-CA concentration at the start of the experiment. These regimes included titrating the ratio of LB to 1x M9 *p*-CA medium initially favoring 100% LB and serially passaging saturated cultures to fresh 80% LB medium containing 20% 1x M9 10 mM *p*-CA medium. Cells were grown aerobically with shaking at 30°C. We gradually increased the percentage of M9 *p*-CA in dilute LB medium. We also tried first growing cells in M9 medium containing both glucose and *p*-CA where the *p*-CA concentration was gradually increased. The third method attempted was by plating cells directly on M9 60 mM *p*-CA plates from saturated overnight LB cultures. The Δ3 strain, the Δ3 Δ*gacA* strain, and a Δ4 (ΔPP_0897 ΔPP_1755 ΔPP_0944 ΔPP_1378) strain were all tested with this passaging regimen with at least 3 biological replicates of each genotype. These strains used and how they were constructed are diagrammed in Figure S2. As arabinose was present in the culture medium, we visually inspected cultures over the duration of this experiment to determine if they still turned blue as a crude indicator of an active indigoidine pathway. Blue forming cultures were only recovered in the Δ3 strain with *p*-CA as the sole carbon source, but not from cultures that also contained glucose. Some clones were recovered in the Δ3 Δ*gacA* background but no longer were blue colored. Many independent lineages were lost upon serial passage and could not be recovered. Other lineages failed to revive on LB plates after short term storage as cryostocks at −80°C.

Peroxide sensitivity assay

P. putida sensitivity to exogenously added hydrogen peroxide was assayed as previously described[56,93] with slight modifications. Briefly, single colonies of the appropriate genotype were struck out from glycerol stocks and inoculated into 5 mL LB cultures and incubated with shaking at 30°C overnight to generate saturated cultures. 3 μL of these cultures were used to inoculate replicate wells in a 48 round well microtiter plate, where each well was prefilled with 300 μL LB medium. Hydrogen peroxide was freshly added to aliquots of LB medium immediately before the plate was prepared at concentrations of 0 mM, 3 mM, and 10 mM from a 30% w/v stock hydrogen peroxide solution (Sigma Aldrich). The results plotted are the average value of three biological replicates, and the banded shaded area represents the standard deviation of the measurements. All experiments were repeated at least one additional time on a different day.

Microbial interaction assay

P. putida WT, Design 1b, and the pre-ALE Δ3 strain were tested for their ability to restore growth in a *P. putida* Δ*fcs* strain using an established microbial interaction assay.[53] Briefly, biomass was first spread from a Δ*fcs* strain in a thick horizontal line down the center of an M9 60 mM *p*-CA agar plate; the potential complementing strain was next spread in a vertical line, intersecting the Δ*fcs* strain in the middle. The plates were incubated at 30°C for 10 days and visually inspected for biomass formation in the Δ*fcs* strain each day.

Soft X-Ray tomography characterization of cells

P. putida WT and Design 1a cells were prepared for soft X-ray tomography (SXT) as follows. Cells were grown either in LB medium or adapted for growth in M9 60 mM *p*-CA medium as for an indigoidine production assay described above. Several hours before cells were to be prepared for SXT, an additional 20% initial volume of fresh medium was added to the cultures to restore consumed nutrients in preparation for transport. Cultures were transferred out of culture tubes and into 50 mL falcon tubes for transit to the National Center for X-ray Tomography (NCXT, LBNL, CA) for cryo-fixation before SXT imaging. Upon arrival, cells were prepared for cryofixation via loading 1–2 μL into pre-cut tapered glass capillaries (∼6um opening) using micro-loaders.[94] The concentration of *P. putida* cells was analyzed using a TC20 Automated Cell Counter (Bio-Rad Laboratories, Hercules, CA). Cells were then harvested by centrifugation at 8000 rpm for 3 min and loaded into capillary tubes using a micro-tip. The prepared specimens in capillary tubes were then plunged frozen into liquid nitrogen cooled liquid propane and then stored in an LN2 Dewar until SXT imaging. Prior to data acquisition, samples were loaded onto a transmission soft X-ray microscope using home-built cryo-transfer apparatus to ensure the integrity of vitrified samples. Data acquisition for 3D tomographic reconstruction was done by taking 2D projections from different angles. The equipped full rotation sample stage rotates with 2-degree increments for 92 projections to ensure an isotropic image reconstruction.[95] SXT data reconstruction without fiducial markers was done by implementing AREC3D,[95] and the auto-segmentation pipeline was based on the CNN training.[96] Cell size and density measurements were manually quantified using the Fiji software package and Amira. For the LB control condition, n = 106 for WT and n = 142 for the Design 1b strain. For the M9 *p*-CA condition, n = 108 for WT and n = 99. N is the number of cells quantified under these conditions. Statistical analysis was performed using a two-tailed unpaired *t* test for the volumetric and density comparisons indicated in the figure to determine if the changes were statistically significant.

Shotgun proteomics analysis

The Design 1a and Design 1b strains and a WT control strain transformed with an empty vector pTE449 plasmid were grown in triplicates in M9 60 mM *p*-CA 50 μg/mL kanamycin using 250 mL shake flasks and back diluted to a starting OD_{600} of 0.05. 8 h post back dilution, the samples were harvested in mid-log phase and stored at −80°C until sample preparation. For the double deletion strain analysis, all combination of double deletion strains and the D1b strain (ΔPP_1378, ΔPP_1755, ΔPP_0944) were grown in quadruplicates in M9 60 mM *p*-CA media using the 24 well deep well plate format and back diluted to a starting OD_{600} of 0.05 and allowed to grow for 8 h until the cell OD_{600} reached 0.8 and similarly harvested and stored at −80°C until analysis. After all samples were collected, protein was extracted from harvested *P. putida* strain cultures and tryptic peptides were prepared by following established proteomic sample preparation procedures.[97] Briefly, cell pellets were resuspended in Qiagen P2 Lysis Buffer (Qiagen Sciences, Germantown, MD, Cat.#19052) for cell lysis. Proteins were precipitated with addition of 1 mM NaCl and 4 x volume acetone, followed by two additional washes with 80% acetone in water. The recovered protein pellet was homogenized by pipetting mixing with 100 mM ammonium bicarbonate in 20% methanol. Protein concentration was determined by the DC protein assay (BioRad Inc, Hercules, CA). Protein reduction was accomplished using 5 mM tris 2-(carboxyethyl)phosphine (TCEP) for 30 min at room temperature, and alkylation was performed with 10 mM iodoacetamide (IAM; final concentration) for 30 min at room temperature in the dark. Overnight digestion with trypsin was accomplished with a 1:50 trypsin:total protein ratio. The resulting peptide samples were analyzed on an Agilent 1290 UHPLC system coupled to a Thermo Scientific Orbitrap Exploris 480 mass spectrometer for discovery proteomics.[98] Briefly, peptide samples were loaded onto an Ascentis ES-C18 Column (Sigma–Aldrich, St. Louis, MO) and separated with a 10 min LC gradient (10% Buffer A (0.1% formic acid (FA) in water) – 35% Buffer B (0.1% FA in acetonitrile)). Eluting peptides were introduced to the mass spectrometer operating in positive-ion mode and were measured in data-independent acquisition (DIA) mode with a duty cycle of 3 survey scans from m/z 380 to m/z 985 and 45 MS2 scans with precursor isolation width of 13.5 m/z to cover the mass range. DIA raw data files were analyzed by an integrated software suite DIA-NN.[99] The database used in the DIA-NN search (library-free mode) is the latest Uniprot *P. putida* KT2440 proteome FASTA sequence plus the protein sequences of heterogeneous pathway genes and common proteomic contaminants. DIA-NN determines mass tolerances automatically based on first pass analysis of the samples with automated determination of optimal mass accuracies. The retention time extraction window was determined individually for all MS runs analyzed via the automated optimization procedure implemented in DIA-NN. Protein inference was enabled, and the quantification strategy was set to Robust LC = High Accuracy. Output main DIA-NN reports were filtered with a global FDR = 0.01 on both the precursor level and protein group level. A jupyter notebook written in Python executed label-free quantification (LFQ) data analysis on the DIA-NN peptide quantification report, and the details of the analysis were described in the established protocol.[100]

TCA metabolite targeted analysis of growth coupled strains

1.5 mL were sampled from liquid cultures in M9 *p*-CA at the 24 h timepoint (or otherwise indicated) of an indigoidine production run and the cell pellets were harvested by centrifugation at 13,000 x *g* for 3 min. Metabolites were quenched with ice-cold 100% methanol, followed by equal volume water for a final concentration of 50% methanol. Quenched metabolites were filtered through a 3,000 Da MW/CO exclusion column (Amicon Ultra, Millipore, Cat. No. UFC500396) by centrifugation at 13,000 x *g* and −2°C for 30-60 min to remove contaminating high molecular weight species above the size cutoff.

Organic acids were measured via reversed-phase chromatography and high-resolution mass spectrometry. Liquid chromatography (LC) was conducted on an Ascentis Express RP-Amide column (150-mm length, 4.6-mm internal diameter, and 2.7-μm particle size; Supelco, Sigma-Aldrich, St. Louis, MO, USA), equipped with the appropriate guard column, using an Agilent Technologies 1260 Series high-performance liquid chromatography (HPLC) system (Agilent Technologies, Santa Clara, CA, USA). A sample injection volume of 2 μL was used throughout. The sample tray and column compartment were set to 5°C and 50°C, respectively. The mobile phase solvents used in this study were of LC-MS grade and purchased from Honeywell Burdick & Jackson (Honeywell, Charlotte, North Carolina, USA). Other chemicals and reagents were purchased from Sigma-Aldrich. The mobile phases were composed of 0.1% FA/84.9% water/15% methanol (v/v/v) (A) and 0.04% FA and 5 mM ammonium acetate in methanol (B). Organic acids were separated via gradient elution under the following conditions: linearly increased from 0% B to 30% B in 5.5 min, increased to 100% B in 0.2 min, held at 100% B for 2 min, decreased from 100%B to 0%B in 0.2 min, and held at 0%B for 2.5 min. The flow rate was held at 0.4 mL/min for 7.7 min, linearly increased from 0.4 mL/min to 1 mL/min in 0.2 min, and held at 1 mL/min for 2.5 min. The total LC run time was 10.4 min. The HPLC system was coupled to an Agilent Technologies 6545 series quadrupole time-of-flight mass spectrometer (QTOF-MS). MS conditions were as follows: Drying and nebulizing gases were set to 10 L/min and 25 lb/in^2, respectively, and a drying-gas temperature of 300°C was used throughout. Sheath gas temperature and flow rate were 330°C and 12 L/min, respectively. Electrospray ionization, via the Agilent Technologies Jet Stream Source, was conducted in the negative ion mode and a capillary voltage of 3,500 V was utilized. The fragmentor, skimmer, and OCT 1 RF Vpp voltages were set to 100, 50, and 300 V, respectively. The acquisition range was from 70 to 1,100 m/z, and the acquisition rate was 1 spectra/sec. The QTOF-MS system was tuned with the Agilent ESI-L Low concentration tuning mix (diluted 10-fold in a solvent mixture of 80% acetonitrile and 20% water) in the range of 50–1700 m/z. Reference mass correction was performed with the Agilent Technologies API-TOF Reference Mass Solution Kit. Data processing and analysis were conducted via Agilent Technologies MassHunter Qualitative Analysis, Profinder, and/or Quantitative Analysis. All other metabolites were analyzed according to the method described by Amer et al.[101] Metabolites were quantified via seven-point calibration curves from 0.39 to 25 μM. To calculate statistical significance, we used an unpaired two tailed *t* test to compare concentrations between the WT control strain and the D1b *glnA* Δ*fleQ* strain. Exact p values are reported and n = 3 biological replicates.

Analytical methods for the quantification of aromatics

All samples were stored at −20°C unless otherwise mentioned. *p*-CA consumption was analyzed by HPLC as previously described.[102] An Eclipse Plus Phenyl-Hexyl column (250 mm length, 4.6 mm diameter, 5 μm particle size, Agilent Technologies) and a Diode Array Detector (G4212, Agilent Technologies) was used to measure UV absorption at 254 nm, 310 nm, and 280 nm. Cultures were centrifuged at 6010 x *g* to remove cells and the extracellular supernatants were used. After all cultures were processed, the supernatant was diluted with mobile phase (10mM ammonium acetate, 0.03% FA) and filtered using a 0.45 μm 96-well microplate (polypropylene membrane, Cat. No. 200983–100, Agilent) by centrifugation for 30 min at 5,250 x *g*. Filtrates were collected in a 96-well plate sealed with an EZ-Pierce film (Cat. No. Z721581, Sigma Aldrich) for analysis by HPLC. Fresh *p*-CA standards were prepared on each day to quantify *p*-CA concentration in the samples. Phenolic compounds were also analyzed according to the LC-MS method as previously described.[103]

Purification of indigoidine used for product quantification and verification of purity by NMR

P. putida KT2440 harboring the integrated indigoidine expression cassette (“WT Control”, or “Control strain”) was used to produce indigoidine which was then used for purification and generation of a standard curve for colorimetric analysis as previously described[31] with slight modifications. Batch to batch variation in commercially procured *p*-CA (Sigma-Aldrich) impacted downstream processing and extraction. Triplicate 50 mL liquid cultures were prepared in baffled shake flasks as described above using M9 60 mM *p*-CA and 1.5% (w/v) arabinose. The cell pellets were harvested after 24 h and washed with a series of solvents from higher to lower polarity for the purification of indigoidine (water, methanol, ethyl acetate, acetonitrile, acetone and hexane). Each wash step consisted of solvent addition, vortexing for ∼1 min and centrifuging at 5,250 x *g* for 5 min to recover indigoidine in the insoluble fraction. Each solvent wash was repeated twice. The resulting product was dried overnight to evaporate residual hexane and the following morning was ground to a fine powder. Purity was confirmed by 1H-Nuclear magnetic resonance (NMR) as described previously.[31]

A standard curve was generated using purified indigoidine generated above. The scale used was calibrated to 25 mg using calibration weights (Troemner, ASTM Class 4) and to account for measurement error. 25 mg aliquots of purified indigoidine were mixed with 25 mL of 100% DMSO in a 50 mL falcon tube and incubated overnight on a shaking platform covered with aluminum foil to ensure total indigoidine solubilization. The reference samples were prepared in triplicate following the triplicate indigoidine samples purified above. Indigoidine absorbance was measured at 612 nm[104] using 1.25-fold serial dilutions of the prepared stock solution to correlate OD_{612} to mg/L indigoidine, and a formula was generated. The formula was: Y = 0.2933x-0.013 and was in good agreement with our previously reported formulae for both *P. putida* and *E. coli* prepared samples from glucose bioconversion processes.

Colorimetric determination of indigoidine from crude sample extracts

200 μL samples were harvested at the designated timepoints and stored at 4°C until samples were batch processed, for no longer than 24 h. When ready, samples were pelleted at 6,010 x g for 3 min using a bench top centrifuge (Eppendorf 5424/5424R). 100% DMSO was added to resuspend the cell pellet with gentle pipetting until the pellet was completely broken down. DMSO resuspended cell pellets were vortexed for 45 min in a Plate Incubator (Cat. No. H6004, Benchmark scientific). Once extraction was completed, the samples were centrifuged at 21,130 x *g* for 1.5 min to remove contaminating cell debris. 100 μL of each sample was added to a 96-well clear flat-bottom plate (Cat. No. 353072, Corning Incorporated) to read absorbance at 612 nm using a microplate reader (SpectraMax M2, Molecular Devices). The standard curve was applied to convert OD_{612} readings into indigoidine titers (g/L). The M9 medium control and WT *P. putida* cell mass does not contribute appreciable signal to the DMSO OD_{612} readings.

LC-MS-based methods for the quantification of indigoidine

DMSO samples quantitated from an indigoidine production run (described in the colorimetric indigoidine method above) were diluted 20x with fresh 100% DMSO. LC was conducted on a Kinetex XB-C18 column (100-mm length, 3.0-mm internal diameter, and 2.6-μm particle size; Phenomenex, Torrance, CA USA) using a 1260 Series HPLC system (Agilent Technologies, Santa Clara, CA, USA). A sample injection volume of 3 μL was used. The sample tray and column compartment were set to 6°C and 50°C, respectively. The mobile phases were composed of 0.4% formic acid (Sigma-Aldrich, St. Louis, MO, USA) in water (A) and 0.4% formic acid in methanol (B). The mobile phase solvents used in this study were of LC-MS grade and purchased from Honeywell Burdick & Jackson (Honeywell, Charlotte, North Carolina, USA). Indigoidine was separated via gradient elution under the following conditions: linearly increased from 10% B to 74.4% B in 4.6 min, linearly increased from 74.4% to 90% in 0.4 min, held at 90%B for 1 min, linearly decreased from 90%B to 10%B in 0.2 min and held at 10%B for 2 min. The flow rate was held at 0.42 mL/min for 5 min, linearly increased from 0.42 mL/min to 0.65 mL/min in 1 min and held at 0.65 mL/min for 2.2 min. The total LC run time was 8.2 min. The HPLC system was coupled to an Agilent Technologies 6520 series quadrupole time-of-flight mass spectrometer (QTOF-MS). Drying and nebulizing gases were set to 11 L/min and 30 lb/in^2, respectively, and a drying-gas temperature of 330°C was used throughout. Electrospray ionization was conducted in the negative ion mode and a capillary voltage of 3,500 V was utilized. The fragmentor, skimmer, and OCT 1 RF Vpp voltages were set to 140, 50, and 250 V, respectively. The acquisition range was from 70 to 1100 m/z, and the acquisition rate was 0.86 spectra/s. The QTOF-MS was tuned with the Agilent Technologies ESI-L low concentration tuning mix in the range of 50–1700 m/z. Reference mass correction was performed with the Agilent Technologies API-TOF Reference Mass Solution Kit (part number G1969-85001) via a second ESI sprayer. Data acquisition and processing were conducted via the Agilent Technologies MassHunter Qualitative Analysis, Profinder, and/or Quantitative Analysis. Metabolites were quantified via a nine-point calibration curve from 1.95 to 500 μM.

Generation of BCD liquor of lignin from [Ch]Lys]-pretreated sorghum

Cholinium lysinate ([Ch][Lys])-based sorghum pretreatment and subsequent saccharification was performed in a one-pot configuration in a 1 L Parr 4520 series Bench Top reactor (Parr Instrument Company, Moline, IL) to obtain solid lignin residues as described previously.[105] 15 wt% 2 mm *Sorghum bicolor* (provided by Idaho National Laboratory), 10 wt% [Ch][Lys], and 75 wt% water were weighed in and pre-mixed in the Parr vessel to obtain a slurry. The obtained slurry was pretreated for 3 h at 140°C with stirring at 80 rpm powered by process (Parr Instrument Company, model: 4871, Moline, IL) and power controllers (Parr Instrument Company, model: 4875, Moline, IL) using three-arm, self-centering anchor with PTFE wiper blades. After 3 h, the pretreated slurry was cooled down and pH was adjusted to 5 with concentrated hydrochloric acid. Enzymatic saccharification of the pH adjusted slurry was carried out at 50°C for 72 h at 80 rpm using enzyme mixtures Cellic CTec3 and HTec3 (9:1 v/v) at a loading of 10 mg protein per g sorghum. After 72 h, the slurry was centrifuged and washed multiple times with DI water to remove any residual sugars and [Ch][Lys]. The washed material was freeze dried to obtain [Ch][Lys]-Sorghum lignin and is fully characterized elsewhere (Wendt et al., manuscript in preparation). This lignin residue was used to generate BCD liquor in a 1 L Parr reactor. Lignin residue (15 wt%) and 5 wt% sodium hydroxide (aqueous solution) were added to the Parr vessel and the temperature was ramped up to 120°C in 30 min. The temperature was held at 120°C for 30 min with vigorous stirring at 80% output of the rotor. After 30 min, the reactor was cooled down and pH was adjusted to 7 with 37% Hydrochloric acid and stored at 4°C until used to replace all double distilled water in 1x M9 BCD liquor medium and sterilized by filter sterilization through a 0.2 μM filter. Major and minor aromatic constituents were characterized using LC-MS and are described in Table S5. Since BCD liquor cannot be autoclaved for sterilization, we added 50 μg/mL chloramphenicol to the medium to inhibit growth of other microorganisms during indigoidine production runs. The resulting BCD liquor was used in place of double distilled H_2O to make M9 minimal salt medium with BCD also substituting for all carbon present. The BCD liquor generation and indigoidine production run was repeated with a second batch of *Sorghum bicolor* and similar results were observed.